

See discussions, stats, and author profiles for this publication at: <https://www.researchgate.net/publication/329611338>

Analyzing Nonlinear Dynamics via Data-Driven Dynamic Mode Decomposition-Like Methods

Article · in Complexity · December 2018

DOI: 10.1155/2018/6920783

CITATIONS
16

READS
252

2 authors:



Soledad Le Clainche
Universidad Politécnica de Madrid

75 PUBLICATIONS 717 CITATIONS

[SEE PROFILE](#)



José M. Vega
Universidad Politécnica de Madrid

211 PUBLICATIONS 2,540 CITATIONS

[SEE PROFILE](#)

Some of the authors of this publication are also working on these related projects:



Higher order dynamic mode decomposition [View project](#)

Review Article

Analyzing Nonlinear Dynamics via Data-Driven Dynamic Mode Decomposition-Like Methods

Soledad Le Clainche and José M. Vega 

E.T.S.I. Aeronáutica y del Espacio, Universidad Politécnica de Madrid, 28040 Madrid, Spain

Correspondence should be addressed to José M. Vega; josemanuel.vega@upm.es

Received 12 June 2018; Revised 11 September 2018; Accepted 24 October 2018; Published 12 December 2018

Academic Editor: J. Nathan Kutz

Copyright © 2018 Soledad Le Clainche and José M. Vega. This is an open access article distributed under the Creative Commons Attribution License, which permits unrestricted use, distribution, and reproduction in any medium, provided the original work is properly cited.

This article presents a review on two methods based on dynamic mode decomposition and its multiple applications, focusing on higher order dynamic mode decomposition (which provides a purely temporal Fourier-like decomposition) and spatiotemporal Koopman decomposition (which gives a spatiotemporal Fourier-like decomposition). These methods are purely data-driven, using either numerical or experimental data, and permit reconstructing the given data and identifying the temporal growth rates and frequencies involved in the dynamics and the spatial growth rates and wavenumbers in the case of the spatiotemporal Koopman decomposition. Thus, they may be used to either identify and extrapolate the dynamics from transient behavior to permanent dynamics or construct efficient, purely data-driven reduced order models.

1. Introduction

Uncovering the quantitative essence of complex signals, either numerical or experimental, coming from nonlinear systems is an interesting topic in *data science* and *fluid dynamics*. Among its several applications in multidisciplinary sciences, the purely data-driven analysis of nonlinear dynamics has raised the interest of applied mathematicians (to understand the dynamics of ordinary or partial differential equations and systems, such as the complex Ginzburg-Landau equation), doctors (to find relevant patterns in medical images), and aeronautical, mechanical, and civil engineers (looking for flow patterns or global instabilities or computing aerodynamic forces on slender or bluff bodies). Even in simple, low-dimensional dynamical systems, such as the Lorenz system (3 ordinary differential equations), it is possible to find complex dynamics, including periodic, quasi-periodic, and chaotic behaviors, as well as complex transients.

Fourier analysis has long been used as a data-processing tool for analyzing complex signals. In addition to improving the standard Fourier transform (e.g., *fast Fourier transform*, *power spectral density* [1], and the so-called *Laskar method* [2, 3]), several techniques have been developed in recent years that extend the scope of Fourier analysis by seeking not

only the frequencies of the signal but also the growth rates, which are relevant to transient behavior. One of the most popular methods to obtain such an expansion is *dynamic mode decomposition* (DMD) [4] (see also [5–7]), which needs to be extended to give optimal results [8], as will be discussed in this paper. These DMD-like methods are based on the idea of decomposing a signal as an expansion in Fourier-like modes, as

$$\mathbf{v}(t) \approx \sum_{n=1}^N a_n \mathbf{u}_n e^{(\delta_n + i\omega_n)t} \quad \text{for } t_1 \leq t \leq t_1 + T, \quad (1)$$

where \mathbf{v} is a time-dependent vector signal, which can be either real or complex, \mathbf{u}_n are conveniently normalized spatial modes, $a_n > 0$ are the mode amplitudes, and δ_n and ω_n are the associated growth rates and frequencies, respectively. Dynamics of the type (1) are paramount in applications, as it will be illustrated in the paper. A good example is the joint wake (accounting for interaction between the individual wakes of the various buildings) of urban topographies; see Figure 1. This example is interesting for two reasons. First, direct numerical simulation is not affordable in realistic conditions due to the huge value of the Reynolds number,

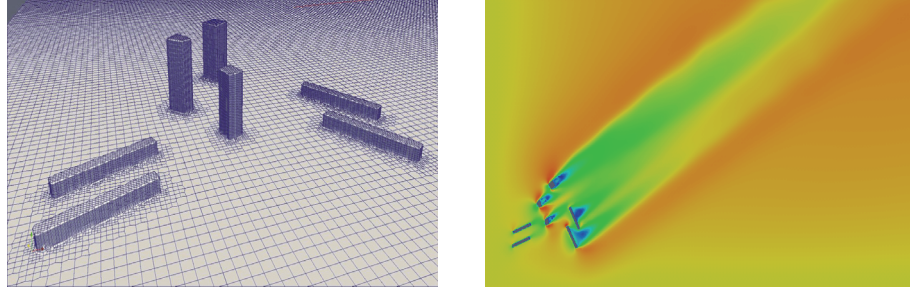


FIGURE 1: An urban topography composed by three skyscrapers and four elongated buildings (left) and horizontal snapshots of the associated joint wake (right).

meaning that numerical data must be obtained using turbulence modeling, which only captures the large scales. These are temporally quasi-periodic and may be described in the form (1); small scales, instead, exhibit spatiotemporal chaos. Experimental data, on the other hand, exhibit nonnegligible errors that must be filtered out and also describe the large scales only.

Expansion (1) is appropriate to represent temporally growing (if $\delta_n > 0$) or decaying (if $\delta_n < 0$), periodic (if the frequencies ω_n are commensurable) or quasi-periodic (if the frequencies are incommensurable) phenomena. Commensurability is a subtle matter in finite precision computations, where exact incommensurability is not possible. Instead, we shall guess that a set of frequencies are incommensurable when the computed values are not commensurable to some small tolerance. Namely, e.g., three frequencies are incommensurable if no relation of the form $m\omega_1 \pm n\omega_2 \pm p\omega_3 = \varepsilon$ is possible for moderate values (say, not larger than 10) of the natural numbers m , n , and p and some small (say, $\sim 10^{-5}$) ε . This can be discerned provided that the frequencies are computed with great accuracy. Moreover, the robustness and accuracy of the approximation (1) are a good means to ensure that the right periodic or quasi-periodic dynamics have been captured. In chaotic dynamics, instead, an infinite number of modes should be considered even for moderate accuracy and the analysis using these methods is subtle.

In the data-driven methods described and used along the paper, space and time will both be discretized. However, it is enlightening to consider at the moment continuous time, with the vector snapshots \mathbf{v} of size J . The simplest problem giving the dynamics in the right hand side of (1) is the ODE linear system

$$\frac{d\mathbf{v}(t)}{dt} = \mathbf{A}\mathbf{v}(t), \quad (2)$$

for an appropriate $J \times J$ matrix \mathbf{A} that may be computed via the pseudoinverse (applied to a discretized version of this equation, considering a collection of nearby snapshots and approximating the time derivative by finite differences).

Obviously, (2) makes sense if the dynamics associated with the snapshots are linear. However, expansion (1) and thus the linear equation (2) also apply to nonlinear dynamics. This is because the linear system (2) only intends to approximate

the particular trajectory in the left hand side of (1), not the complete dynamics of the nonlinear system. In other words, if a different trajectory of the nonlinear system is given, for different initial conditions, matrix \mathbf{A} is also generally different. In any event, for generic \mathbf{A} , all solutions of (2) are of the form displayed in the right hand side of (1), where the modes \mathbf{u}_n are the eigenvectors of \mathbf{A} and $\delta_n + i\omega_n$ are the associated eigenvalues. However, not all expansions of form (1) are solutions of (2) because (2) provides at most J modes, while the number of terms involved in (1), N , which is known as the *spectral complexity* of expansion (1), can be larger than J . More precisely, defining the *spatial complexity* of expansion (1), $M \leq J$, as the dimension of the span of the modes $\mathbf{u}_1, \dots, \mathbf{u}_N$, the linear problem (2) is appropriate to compute (1) only if $M = N$ (note that M cannot be larger than N). We insist here that the spectral and spatial complexities are defined for expansion (1), not for the dynamical system from which the snapshots may come. However, $N > M$ in many dynamical systems of scientific/technological interest, such as the following:

- (i) The *Lorenz system* [9] (and other ODEs) in which $M = 3$, while N may be quite large
- (ii) Many *nonlinear, infinite-dimensional dynamical systems* (PDEs) exhibiting an *inertial manifold* [10] (limited M) but complex (e.g., quasi-periodic) temporal behavior
- (iii) *Extrapolating* from transients to obtain attractors [11] requiring identifying additional (temporally decaying modes), which increases N
- (iv) *Experimental noise/numerical errors* adding (unphysical) temporal complexity that increases N and must be identified to *clean the postprocessed data*

When $N > M$, the number of involved modes is increased by using a higher order ODE system. Specifically the linear system (1) can be replaced by

$$\begin{aligned} \frac{d^d \mathbf{v}}{dt^d} = \mathbf{A}_1 \frac{d^{d-1} \mathbf{v}(t)}{dt^{d-1}} + \mathbf{A}_2 \frac{d^{d-2} \mathbf{v}(t)}{dt^{d-2}} + \cdots + \mathbf{A}_{d-1} \frac{d \mathbf{v}(t)}{dt} \\ + \mathbf{A}_d \mathbf{v}(t), \end{aligned} \quad (3)$$

for appropriate $J \times J$ matrices $\mathbf{A}_1, \dots, \mathbf{A}_d$. Obviously, this linear problem can also be written in the form (3), as

$$\frac{d\tilde{\mathbf{v}}}{dt} = \mathbf{A}\tilde{\mathbf{v}}. \quad (4)$$

Here, $\tilde{\mathbf{v}}$ is a vector of size Jd that collects \mathbf{v} , $d\mathbf{v}/dt, \dots$, and $d^{d-1}\mathbf{v}/dt^{d-1}$, and the $(Jd) \times (Jd)$ -matrix \mathbf{A} is a sparse matrix whose blocks are the unit $J \times J$ -unit matrix and the matrices $\mathbf{A}_1, \dots, \mathbf{A}_d$. The matrix \mathbf{A} can be computed via the pseudoinverse applied to $\tilde{\mathbf{v}}(t)$. Now, for an appropriate value of the index d , any dynamics of the form displayed in the right hand side of (1) can be captured. Note that the size of the matrix \mathbf{A} is huge when J and d are both large, which would require very large computational resources. However, these resources are greatly decreased by applying this idea after appropriate dimension reduction; see below.

In the discrete counterpart of (1), the time variable is discretized at K equispaced values of t , as $t_k = t_1 + (k-1)\Delta t$, with $\Delta t = T/K$, and a set of snapshots is defined as $\mathbf{v}_k = \mathbf{v}(t_k)$. The counterparts of (1), (2), and (3) are

$$\mathbf{v}_k \simeq \sum_{n=1}^N a_n \mathbf{u}_n e^{(\delta_n + i\omega_n)t_k} \quad \text{for } k = 1, \dots, K, \quad (5)$$

$$\mathbf{v}_{k+1} = \mathbf{R}^t \mathbf{v}_k \quad \text{for } k = 1, \dots, K-1, \quad (6)$$

$$\mathbf{v}_{k+d} = \mathbf{R}_1^t \mathbf{v}_{k+d-1} + \mathbf{R}_2^t \mathbf{v}_{k+d-2} + \dots + \mathbf{R}_d^t \mathbf{v}_k \quad (7)$$

$$\text{for } k = 1, \dots, K-d,$$

respectively. Obviously, (1) follows from (5) by just setting t_k continuous (interpolation in t). Interpolation can also be made in the spatial variable, which yields the continuous *temporal DMD* expansion (cf. (1)):

$$\mathbf{v}(\mathbf{x}, t) \simeq \sum_{n=1}^N a_n \mathbf{u}_n(\mathbf{x}) e^{(\delta_n + i\omega_n)t} \quad \text{for } t_1 \leq t \leq t_1 + T, \quad (8)$$

where the modes \mathbf{u}_n depend on the spatial variable and the vector \mathbf{v} may account for a vector state variable, such as the velocity vector in fluid flows.

Equation (6) is the essence of *standard DMD* [6] that, as explained above, only applies when the spatial and spectral complexities coincide. Equation (7), instead, is the basis of *higher order DMD* (HODMD) [8]. This method permits computing the expansion (1) in the general case $M < N$ choosing an appropriate value of the tunable index d . Note that the main difference between (6) and (7) is that the latter equation relates each snapshot with not only the last snapshot but also the former $d-1$ snapshots. In fact, HODMD reduces to standard DMD if $d = 1$. For $d > 1$, instead, HODMD can be seen as a result of applying standard DMD to a set of enlarged snapshots containing also the delayed snapshots. Thus, HODMD synergically combines the advantages of standard DMD and some consequences [12] of the delayed embedding theorem by Takens [13], who followed and formalized former seminal ideas by Packard et al. [14]. In fact, combination of DMD and delayed snapshots had previously been suggested [7] and performed [15], in a

spirit different from that in [8]. Other applications of Takens' theorem in different contexts (not related to DMD) include, e.g., modal parameter identification and model reduction [16], identification of invariant sets and bifurcations from time-series [17], and analysis of high-dimensional time-series combining the Laplacian eigenmaps with time-lagged embedding [18]. On the other hand, some of the many improvements of standard DMD based on different ideas (not related to time-lagged snapshots) are as follows:

- (i) Optimized DMD [19], in which the expansion is computed via an optimization problem. Compared to this method, standard DMD and HODMD are simpler, purely linear algebra driven approaches. However, some linear algebra oriented (and thus less computationally expensive) approaches have been developed to treat separable nonlinear least squares problems [20], in particular, that involved in optimized DMD [21].
- (ii) Sparsity promoting DMD [22], which uses a penalty to identify a smaller set of important modes via convex optimization techniques.
- (iii) Extended DMD [23], which extends the standard DMD approximation to include more basis functions, allowing the method to capture more complex behavior.
- (iv) Total least squares DMD [24], which combines total least squares and standard DMD to treat noisy data. Let us mention here that other improvements of standard DMD have been developed to correct the effect of noise. Among these, Dawson et al. [25] also tried to characterize the noise properties, Takeishi et al. [26] combined a Bayesian formulation with DMD, and Dicle et al. [27] computed low-rank factors of the DMD operator while satisfying the total least squares constraints.

On the other hand, for spatially developing flows, t may be replaced in (8) by a distinguished spatial variable x , obtaining the *spatial DMD expansion*

$$\mathbf{v}(x, y, t) = \sum_{m=1}^M a_m \mathbf{u}_m(y, t) e^{(\nu_m + i\kappa_m)x}, \quad (9)$$

where y collects the remaining transversal spatial variables and ν_m and κ_m are the spatial growth rates and wavenumbers, respectively. Still, a simultaneous exponential behavior in space and time may be relevant, considering the *spatiotemporal Koopman decomposition* (STKD) [28]

$$\mathbf{v}(x, y, t) = \sum_{m=1}^M \sum_{n=1}^N a_{mn} \mathbf{u}_{mn}(y) e^{(\nu_m + i\kappa_m)x + (\delta_n + i\omega_n)t}, \quad (10)$$

which will be obtained by an appropriate STKD method described below. This method roughly consists in applying HODMD along the x and t coordinates simultaneously. Expansion (10) has been attempted in [29] in a data-driven fashion, through an approach based on Koopman operator

theory plus the use of appropriate basis functions. See also the analysis in [30], where some aspects of the theory of operator-valued kernels for machine learning with delay-coordinate maps of dynamical systems are combined. Similar spatiotemporal expansions have also been already derived (via a not purely data-driven method) for the Navier-Stokes (NS) equations in [31] by first projecting the NS equations into the temporal modes and then applying spatial DMD to these modes using appropriate basis functions.

The modes $\mathbf{u}_{mn}(\mathbf{y})$ are appropriately normalized and expansion (10) will be further truncated by retaining only those modes whose amplitudes a_{mn} are larger than a given threshold. In other words, expansion (10) will not generally contain the $M \times N$ modes indicated in (10), but a smaller number of modes, which is emphasized rewriting (10) as

$$\mathbf{v}(x, \mathbf{y}, t) = \sum_{m,n} a_{mn} \mathbf{u}_{mn}(\mathbf{y}) e^{(\gamma_m + i\kappa_m)x + (\delta_n + i\omega_n)t}. \quad (11)$$

It is interesting to note that the methods considered above are related to former seminal ideas by Koopman [32]; see also [5, 31, 33]. *Koopman operator theory* is concerned with *observability* in dynamical systems. Specifically, for a dynamical system $\mathbf{v}(t)$, we may consider the temporal shift $t \rightarrow t + \Delta t$, with fixed Δt . For an arbitrary vector observable function \mathbf{g} , the Koopman operator \mathbf{R}^t is defined as

$$(\mathbf{R}^t \cdot \mathbf{g})(\mathbf{v}(t)) = \mathbf{g}(\mathbf{v}(t + \Delta t)). \quad (12)$$

This operator is linear, because obviously $\mathbf{R}^t \cdot (\alpha_1 \mathbf{g}_1 + \alpha_2 \mathbf{g}_2) = \alpha_1 \mathbf{R}^t \cdot \mathbf{g}_1 + \alpha_2 \mathbf{R}^t \cdot \mathbf{g}_2$, and infinite-dimensional, since it acts on the infinite-dimensional space of observables. Thus, its eigenvalues and eigenvectors allow for giving an exact representation of any observable. Setting \mathbf{g} =the identity, the Koopman operator (12) reduces to (6) and is thus related to the standard DMD method. Similarly, considering an observable that also takes into account delayed snapshots, the Koopman operator reduces to (7) and is thus related to HODMD. Still, particular realizations of the spatiotemporal Koopman operator $\mathbf{R}^{x,t}$, defined as

$$(\mathbf{R}^{x,t} \cdot \mathbf{g})(\mathbf{v}(x, \mathbf{y}, t)) = \mathbf{v}(x + \Delta x, \mathbf{y}, t + \Delta t), \quad (13)$$

are related to the STKD method mentioned above. This connection is why we call this method spatiotemporal Koopman decomposition.

Finally, we note that in the weakly nonlinear analysis of oscillatory pattern forming systems [34, 35], some equations similar to (9) and (10) are also obtained. However, these methods require both knowing the governing equations and assuming that the dynamics are small perturbations of a known steady or periodic solution. In contrast, DMD, HODMD, and STKD provide approximations of type (9) and (10) in a purely data-driven fashion for arbitrary fully nonlinear dynamics, which are great advantages, specially in the case of the analysis of experimental data. Note in this context that expansions (9) and (10) can be seen as *semianalytical expressions* that allow for the fast online computation of the associated spatiotemporal data, which leads to a *purely data-driven reduced order model* (ROM). Among the most

important applications of such a ROM, (i) it avoids numerical computation, which may be quite computationally expensive in large scale systems, or even not possible when the model is obtained from experimental data; (ii) it predicts different flow states through available data reducing the number of data collected in experiments; and (iii) it provides efficient tools for various applications, including flow control [36] and optimization design [37].

With the above in mind, the main object of this paper is to present the HODMD and STKD methods, illustrating them in simple toy models and applying them to various problems of scientific and technological interest. To this end, the HODMD method is described and illustrated in a simple toy model in Section 2, while several applications of this method are considered in Section 3. The STKD method is developed in Section 4 and applied to various problems in Section 5. The paper ends with some concluding remarks in Section 6.

2. Higher Order Dynamic Mode Decomposition

As above, for a time-dependent dynamical system given by the vector state variable $\mathbf{v}(t)$, of size J , we consider a set of K snapshots at equispaced values of t ,

$$\mathbf{v}_k = \mathbf{v}(t_k), \quad (14)$$

with $t_k = t_1 + (k - 1)\Delta t$ for $k = 1, \dots, K$.

If the dynamical system is infinite-dimensional, the finite-dimensional state vector \mathbf{v} generally results from spatial discretization. The snapshots are organized in a snapshot matrix (whose columns are the snapshots), as

$$\mathbf{V}_1^K = [\mathbf{v}_1, \mathbf{v}_2, \dots, \mathbf{v}_K]. \quad (15)$$

In the sequel, the accuracy of the various approximations of the snapshots will be measured in terms of the *relative root mean square* (RMS) error, defined as

$$\text{RRMS error} = \sqrt{\frac{\sum_{k=1}^K \|\mathbf{v}_k^{\text{approx}} - \mathbf{v}_k\|_2^2}{\sum_{k=1}^K \|\mathbf{v}_k\|_2^2}}, \quad (16)$$

where $\|\cdot\|_2$ denotes the usual Euclidean norm. The right hand side of (16) measures the collective RMS error in space and time normalized with the spatiotemporal RMS norm of the snapshots. Obviously, other norms (omitted here for the sake of brevity) would be more appropriate when the dynamics exhibit disparate localized behavior in space and/or time.

For simplicity, only the temporal expansion (5) will be considered in this section. The spatial expansion (9) is obtained by just interchanging the roles of x and t .

2.1. The HODMD Method. The HODMD algorithm proceeds in two steps (see [8] for more details).

Step 1 (dimension reduction). Applying truncated *singular value decomposition* (SVD) [38] to the snapshot matrix \mathbf{V}_1^K yields

$$\mathbf{V}_1^K \simeq \mathbf{P} \Sigma \mathbf{Q}^\top \equiv \mathbf{P} \widehat{\mathbf{T}}_1^K \quad (\text{or } \mathbf{v}_k = \mathbf{P} \widehat{\mathbf{t}}_k), \quad (17)$$

with $\widehat{\mathbf{T}}_1^K = \Sigma \mathbf{Q}^\top$,

where the matrix $\widehat{\mathbf{T}}_1^K$ is known as the dimension-reduced snapshot matrix and their columns, the *dimension-reduced snapshots*, $\widehat{\mathbf{t}}_k$. The number of retained modes, which is the spatial complexity defined above, M , is determined by a (tunable) tolerance ε_1 , requiring that the RRMS error of the approximation, as defined in (16), be smaller than ε_1 ; this error is easily computed in terms of the singular values using well-known SVD formulae [38]. For noisy data we may choose ε_1 comparable to the noise level, which helps to clean the data [39]. Now we note that if we had a DMD expansion for the dimension-reduced snapshots, as

$$\widehat{\mathbf{t}}_k \simeq \sum_{n=1}^N a_n \widehat{\mathbf{u}}_n e^{(\delta_n + i\omega_n)t_k} \quad \text{for } k = 1, \dots, K, \quad (18)$$

which in fact will be computed in the next step, substituting this expansion into (17) (namely, premultiplying (18) by the matrix \mathbf{P}), then we obtain the DMD expansion (5) we are looking for.

Step 2 (the DMD-d algorithm for the dimension-reduced snapshots). Now, we must treat the standard DMD and the HODMD algorithms separately. For ordinary DMD, we consider the Koopman assumption (6) for the dimension-reduced snapshots, which reads

$$\widehat{\mathbf{t}}_{k+1} \simeq \widehat{\mathbf{R}}^t \widehat{\mathbf{t}}_k, \quad (19)$$

where the $M \times M$ matrix $\widehat{\mathbf{R}}^t$ (reduced *Koopman matrix*) is computed from the dimension-reduced snapshots via the pseudoinverse. Now, the reduced expansion (18) is computed as follows. The reduced modes $\widehat{\mathbf{u}}_n$ are normalized eigenvectors of $\widehat{\mathbf{R}}^t$, the exponents are related to the eigenvalues, μ_n , as $\delta_n + i\omega_n = \log \mu_n / \Delta t$, and the amplitudes a_n are computed via least squares fitting (as in optimized DMD [19]) of the dimension-reduced snapshots in expansion (18). This completes the algorithm for standard DMD.

Concerning HODMD, the counterpart of (6) for the reduced snapshots,

$$\widehat{\mathbf{t}}_{k+d} \simeq \widehat{\mathbf{R}}_1 \widehat{\mathbf{t}}_{k+d-1} + \widehat{\mathbf{R}}_2 \widehat{\mathbf{t}}_{k+d-2} + \dots + \widehat{\mathbf{R}}_d \widehat{\mathbf{t}}_k, \quad (20)$$

is treated using the *enlarged snapshots*

$$\widetilde{\mathbf{t}}_k \equiv \begin{bmatrix} \widehat{\mathbf{t}}_k \\ \widehat{\mathbf{t}}_{k+1} \\ \vdots \\ \widehat{\mathbf{t}}_{k+d-2} \\ \widehat{\mathbf{t}}_{k+d-1} \end{bmatrix}. \quad (21)$$

Applying Step 1 above (a second dimension reduction that eliminates redundancies between the snapshots and delayed snapshots) gives a new set of enlarged dimension-reduced snapshots, $\widetilde{\mathbf{t}}_k$, which are assumed to satisfy the counterpart of (19), namely, $\widetilde{\mathbf{t}}_{k+1} \simeq \widetilde{\mathbf{R}} \widetilde{\mathbf{t}}_k$, where the matrix $\widetilde{\mathbf{R}}$ is computed via the pseudo inverse, as above. The eigenvalues of eigenvectors of $\widetilde{\mathbf{R}}^t$ permit obtaining the counterpart of (18) for the enlarged dimension-reduced snapshots. Considering only the first M components in this expansion, we obtain the dimension-reduced expansion (18), where the mode amplitudes a_n are computed via least square fitting with the dimension-reduced snapshots, which completes the derivation of (18) in the HODMD method.

Once expansion (18) has been computed either for standard DMD or for HODMD, the expansion is sorted in decreasing order of the mode amplitudes and is further truncated by eliminating those modes such that

$$\frac{a_n}{a_1} < \varepsilon_2, \quad (22)$$

for some tunable parameter ε_2 .

Some remarks about the method are now in order:

- (i) A solver for the DMD-d algorithm described above can be found in [40].
- (ii) It is interesting to note that the enlarged snapshots, containing also the delayed snapshots, are defined for the reduced snapshots (whose size is M), not for the (usually much larger) original snapshots, which, as anticipated, would greatly increase the computational cost of the method. In fact, the ratio of the computational cost of HODMD to that of standard DMD scales with a first or second power (depending on the comparative values of J , Md , and K) of $J/(Md)$, which is of order one in most applications (but obviously not always).
- (iii) Considering periodic or quasi-periodic dynamics, and measuring the accuracy of the DMD reconstruction with the RRMS error defined in (16), the method is quite robust in connection with the tunable parameters d , ε_1 , and ε_2 . In particular, the plot of the RRMS error versus d is fairly flat near the minimum, which means that the selection of d is not critical. In principle, if the data were exact, the smaller ε_1 and ε_2 , the better the approximation. However, in the presence of noise or discretization/truncation errors, ε_1 and ε_2 must be not too small to avoid that the method captures unphysical modes. In other words, these two parameters must be comparable to the noise/errors level, but see the next remark. Finally, the timespan $t_K - t_1$ and the time shift between snapshots, Δt , must be selected as somewhat larger and smaller than the largest and smallest involved periods, respectively.
- (iv) An obvious trade-off of the HODMD method is that we have an additional tunable parameter d , which

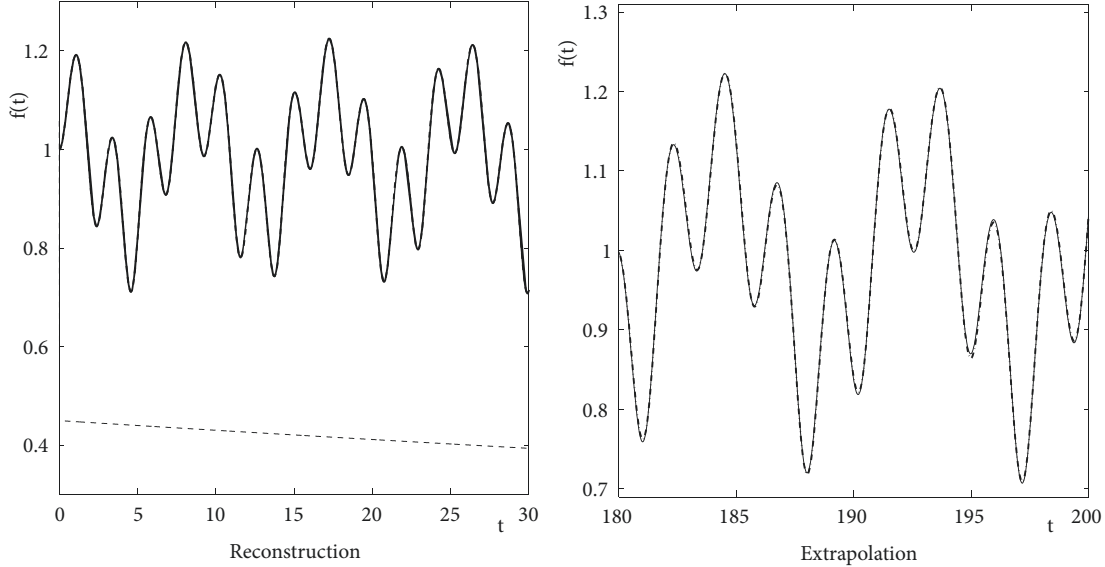


FIGURE 2: Toy model function defined in (16) (thin solid lines) and the reconstruction using DMD-800 (thick dashed lines) and DMD-1 (thin dashed line).

is not present in standard DMD and must be chosen via trial-and-error. However, as explained above, the method is robust in connection with the parameter d .

- (v) The parameters ε_1 and ε_2 can be seen as governing spatial and temporal truncation, respectively. For finite accuracy and given values of the tunable parameters, a new application of the method to the HODMD reconstructed solution does not necessarily give the same reconstruction. This is specially interesting for noisy data, in which the iterative application of the method (*iterative HODMD*, see [41]) improves noise filtering (beyond the well-known [39] noise filtering effect associated with the application of truncated SVD in Step 1). It is to be noted that iterating HODMD with fixed tolerances ε_1 and ε_2 eliminates both spurious SVD modes and spurious DMD frequencies, decreasing along the iterations both the spatial and spectral complexities, M and N , respectively. The iteration is terminated when M and N do not decrease further. By choosing ε_1 and ε_2 comparable to the noise level, the method permits uncovering physical phenomena that were masked by noise in the original data. A striking example of the ability of the iterative HODMD method to filter noise and uncovering the physically relevant dynamics will be given in Section 3.2.

- (vi) When more than one spatial coordinate is present, and spatial discretization is made in a structured mesh in some of the spatial coordinates, the given data can be organized in a *snapshot tensor* instead of a snapshot matrix. In this case, standard DMD can be substituted in Step 1 (see [41]) by HOSVD [42], a well-known extension of standard DMD by Tucker [43]. HOSVD decomposes the tensor as a linear

combination of tensor products of modes in the various directions. The DMD- d algorithm is applied separately (perhaps with different values of d) to the various sets of modes.

2.2. Illustration of the HODMD Method in a Toy Model. Let us first illustrate the method in the following quasi-periodic simple toy model

$$\nu(t) = \sqrt{1 + \frac{1}{2} \sin t \sin(\sqrt{3}t)}. \quad (23)$$

This model exhibits the incommensurable fundamental frequencies $\sqrt{3} \pm 1$, which are somewhat disparate from each other and their joint harmonics. The spatial complexity is $M = 1$, while the spectral complexity N (which increases as the accuracy of the reconstruction is required to be more and more strict) is larger than one. The convenience of using delayed snapshots when the spatial complexity is 1 was already mentioned in [7]. The HODMD algorithm DMD-800 is applied to a set of $K = 2000$ snapshots in the timespan $0 \leq t \leq 32$, with tolerances $\varepsilon_1 = 10^{-10}$ and $\varepsilon_2 = 10^{-4}$. The method identifies $N = 27$ frequencies and reconstructs the snapshots with RRMS error, as defined in (16), $\sim 2 \cdot 10^{-4}$ in this interval. Thus, the original quasi-periodic function and its reconstruction are plot-indistinguishable (see Figure 2-left). Moreover, the extrapolation of this reconstruction to the interval $180 \leq t \leq 200$ (Figure 2-right) is still quite good, since the RRMS error is $\sim 2.7 \cdot 10^{-3}$. On the contrary, the standard DMD algorithm DMD-1 (Figure 2-left, thin dashed line) identifies just one spurious frequency and gives a $O(1)$ RRMS error.

More realistic applications of the HODMD method and its iterative extension are considered in the next section.

3. Applications of HODMD

The discussion about spectral and spatial complexities is a key point to understand the wide range of applications of HODMD. As anticipated in Section 1 and further explained in [11], there are several natural cases in which the spectral complexity is larger than the spatial complexity. Here, we shall concentrate on two such cases, one driven by numerical data from the complex Ginzburg-Landau equation (CGLE) and another by experimental data from the zero-net-mass-flux (ZNMF) jet, which will be considered in Sections 3.1 and 3.2, respectively. Additional applications will be briefly addressed in Section 3.3.

3.1. Application to the CGLE. Let us consider the following CGLE with periodic boundary conditions:

$$\partial_t A = (1 + i\alpha) \partial_{xx}^2 A + \mu u - (1 + i\beta) |A|^2 A, \quad (24)$$

$$\begin{aligned} A(-1, t) &= A(1, t), \\ \partial_x A(-1, t) &= \partial_x A(1, t). \end{aligned} \quad (25)$$

The dependent variable A is complex and can be seen as the *complex amplitude* when using (24) as the weakly nonlinear “normal form”, which applies at the onset of oscillatory instabilities in many relevant physical systems [34, 35]. The CGLE is a well-known paradigm of pattern forming systems that exhibits complex dynamics [44] due to the modulational instability if $\alpha\beta < -1$ (Newell’s condition [44]) and μ exceeds a threshold value. For typical values of α , β , and μ , the CGLE possesses an inertial manifold contained in a linear subspace of dimension 20-30 (upper limit of the spatial complexity), while the dynamics may be complex, meaning that the spectral complexity can be large. Thus, the standard DMD-1 algorithm fails except for the simplest monochromatic attractors [8].

Problem (24)-(25) is invariant under the $O(2) \times SO(2)$ symmetry group generated by spatial translations and reflections, and phase shifts in A ,

$$\begin{aligned} x &\longrightarrow x + c_1, \\ x &\longrightarrow -x, \\ A &\longrightarrow Ae^{ic_2}. \end{aligned} \quad (26)$$

Because of the latter symmetry, it is convenient to write down expansion (1) for the CGLE as

$$A(x, t) = e^{i\omega_0 t} \sum_{n=1}^N a_n u_n(x) e^{i\omega_n t}, \quad (27)$$

where the frequencies $\omega_1, \omega_2, \dots$ are linear combinations with integer coefficients of some fundamental frequencies, which are generally incommensurable with ω_0 . Thus, the dynamics of A are more complex than those of $|A|$. In other words, A is periodic if $|A|$ is stationary, and A represents a 2-torus if $|A|$ is periodic. In the sequel, we consider just two attractors, one

such that $|A|$ is periodic and another such that $|A|$ is quasi-periodic. Both attractors are obtained for

$$\begin{aligned} \alpha &= -10, \\ \beta &= 10, \end{aligned} \quad (28)$$

and two values of μ . Note that since $|\alpha|$ and $|\beta|$ are both somewhat large, dispersion and nonlinear detuning are large compared to diffusion and nonlinear damping, respectively, which is demanding from the computational point of view and promotes complex dynamics. For the construction of the databases, the equation is solved numerically using a Crank-Nicolson plus Adams-Basforth scheme [45] for temporal discretization, with time step $\Delta t = 10^{-5}$, while the second-order spatial derivative is discretized using centered finite differences in a uniform grid of 1000 points. HODMD is applied to a set of 2000 snapshots, collected in an appropriate time interval of length 1, disregarding a transient time-stage. In the two cases considered below, a good value of the index d when applying the HODMD algorithm is $d = 50$, while the remaining tunable parameters are $\varepsilon_1 = 10^{-8}$ and two values of ε_2 , namely,

$$\begin{aligned} \varepsilon_2 &= 5 \cdot 10^{-3} \text{ (high accuracy)}, \\ \varepsilon_2 &= 10^{-4} \text{ (low accuracy)}. \end{aligned} \quad (29)$$

Selecting these values of the tunable parameters as common for the two cases considered below illustrates the robustness of the method, which is further checked noting that low and high accuracy computations are consistent among each other, and the results coincide when different timespans are used in the computations.

The first case to be considered in that for $\mu = 20$, in which using the DMD-50 algorithm, the RRMS reconstruction error (see (16)) is $\sim 6 \cdot 10^{-3}$ and $\sim 2 \cdot 10^{-5}$ for low and high accuracy, respectively, retaining 6 and 12 DMD modes, respectively. The semilogarithmic plot of the DMD amplitude versus frequency is plotted in Figure 3-left, where it can be seen that the relevant points are approximately contained in two straight lines centered at $\omega_0 = 11.6$, which means that expansion (27) converges spectrally; using the standard DMD method (DMD-1 algorithm), instead, gives spurious results, plotted with red symbols in the figure. The remaining points obtained via the DMD-50 algorithm lie equispaced in frequency, with a distance between them equal to $\omega = 118.7$, which means that the frequencies ω_n appearing in expansion (27) are all (positive or negative) harmonics of ω . Thus, $|A|$ is time-periodic (see Figure 3, middle), with a period $2\pi/\omega$, while A is quasi-periodic (2-torus), with fundamental frequencies ω_0 and ω . Since ω_0 is small compared to ω the pattern is slowly modulated (Figure 3, right). The spatial modes appearing in the expansion (27), u_n , which are not plotted for the sake of brevity, exhibit a reflection symmetry around $x = -0.17$ (indicated with a vertical white line in Figure 3), meaning that the whole pattern also exhibits this symmetry, consistently with the invariance of the problem under the actions (26). This implies that the pattern can be seen as a standing wave (SW), as indicated with the vertical

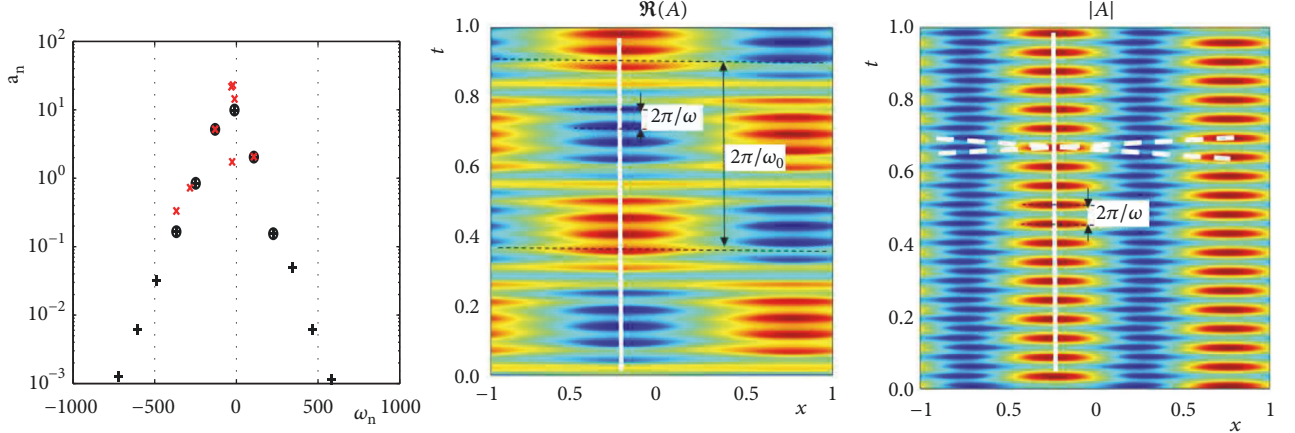


FIGURE 3: The CGLE for $\mu = 20$, plotting the amplitudes versus frequencies in the DMD expansion (left plot) for low (black circles) and high (black crosses) accuracy computations using DMD-50, and using DMD-1 (red symbols), and the color map of $\Re(A)$ (middle plot) and $|A|$ (right plot).

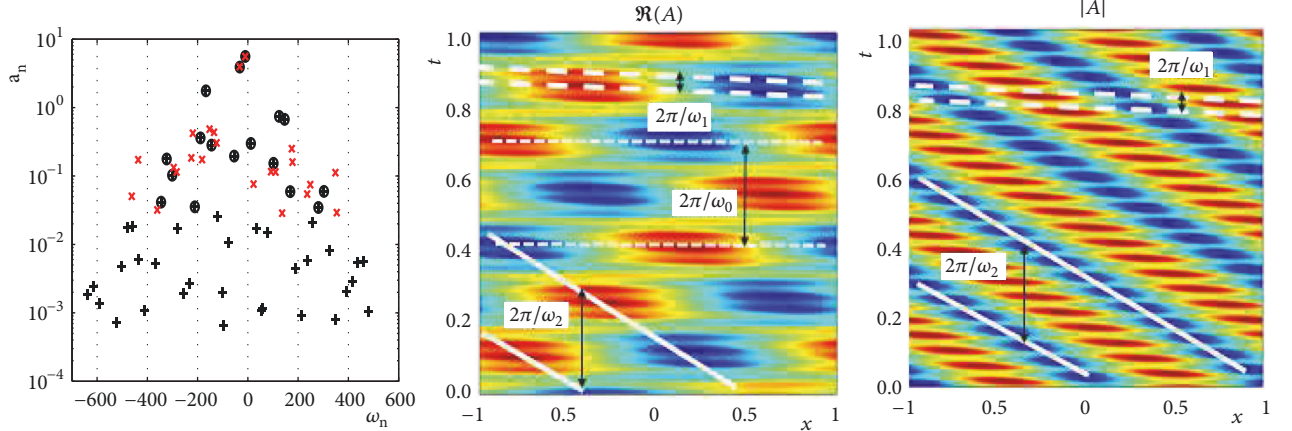


FIGURE 4: Counterpart of Figure 3 for $\mu = 22$.

while solid line in Figure 3, but it can also be considered as either a right or left traveling wave (TW), as indicated with the oblique dashed lines in this figure. This dual interpretation cannot be ascertained from the shape of the modes u_n , but this issue will be revisited and further checked in Section 5.1.

As a second case, we consider the value $\mu = 22$ (Figure 4), in which the dynamics are more complex. Again, the DMD-1 algorithm yields spurious results. Instead, for low and high accuracy (see (29)), the DMD-50 algorithm retains 17 and 49 modes, giving a RRMS reconstruction error (see (16)) $\sim 8 \cdot 10^{-3}$ and $\sim 2 \cdot 10^{-4}$, respectively. The main difference with the case considered in Figure 3 is that now the plot of the amplitude versus the frequency forms a triangular pattern that also decays spectrally but shows that, in addition to $\omega_0 = -21.2$, the frequencies in the expansion in the right hand side of (27) are linear combinations with integer coefficients of the fundamental frequencies $\omega_1 = 156.6$ and $\omega_2 = 22.2$, which are not easily identified in Figure 4, left. Thus, guessing that the three fundamental frequencies are incommensurable, the attractor for $|A|$ is contained in a 2-torus while that for A lies in a 3-torus. Finally, the middle and right plots in Figure 4

show that the pattern is a TW but, as in the former case, elucidating this issue from the shape of the modes $u_n(x)$ appearing in (27) turns out to be a difficult (and unnatural) issue. The STKD method, which will be applied to the CGLE in Section 5.1, instead, will solve this issue in a natural way.

In summary, the HODMD method is able to precisely compute the temporal DMD expansion for the CGLE, giving robust results and distinguishing between periodic and quasi-periodic phenomena. However, identifying SWs and TWs requires additional ingredients, which will be included in the STKD method, developed in Section 4 and applied to the CGLE in Section 5.1.

3.2. Application to the Zero-Net-Mass-Flux Jet. A zero-net-mass-flux (ZNMF) jet [46, 47] is a pulsatile jet promoted by a piston or membrane that interchanges fluid flow through an orifice with an outer ambient fluid that is at rest far from the orifice. The net mass flux is zero, but at large Reynolds number there is a nonzero (and large) net flux of momentum that, in addition to its own scientific interest, is useful in various fields. For instance, synthetic jet actuators promote pulsatile

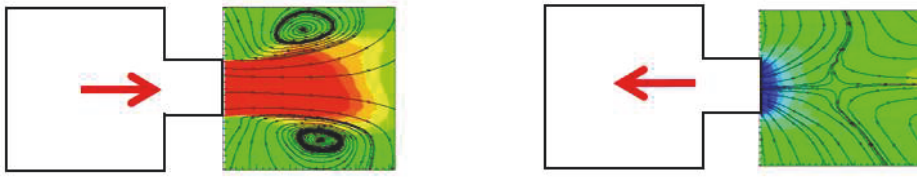


FIGURE 5: Pseudo-streamlines in a meridional section for two representative snapshots of the injection (left) and suction (right) phases in the ZNMF jet.

jets [48] that are useful in, e.g., mixing enhancement [49], jet vectoring [50], heat transfer [51], and active flow control of boundary layer separation [52]. These jets are also relevant in nature, in connection with squid, octopus, salp, and jellyfish swimming [53].

It must be noted that the nonzero momentum flux at large Reynolds number is due to the fact that, even if the periodic forcing is temporally reflection symmetric, the flow is highly nonreflection symmetric, as illustrated in Figure 5, where an approximately rotationally symmetric jet produced by a circular orifice is considered. As can be seen, a vortex ring is formed in the injection phase that travels downstream, while the suction phase is characterized by a saddle point that separates the fluid reentering the cavity from that still moving downstream.

The ZNMF jet promotes a complex flow structure that involves various, disparate spatiotemporal scales, whose understanding remains as an open topic. Thus, this is a convenient problem to test the performance of the HODMD method. Also, in order to test the noise filtering ability of the iterative HODMD method, the analysis will be based on experimental data resulting from particle image velocimetry (PIV), as obtained [46, 47] in the experimental facility for ZNMF jets of the Laboratory for Turbulence Research and Combustion at Monash University. Such measurements exhibit an error $\sim 2.4\%$ at the 95% confidence level. Two nondimensional parameters characterize the flow conditions, namely the *Reynolds* and *Strouhal numbers*, defined as $\text{Re} = UD/\nu$ and $\text{St} = fD/U$, respectively, where D is the jet orifice diameter, ν is the kinematic viscosity, U is related to the peak oscillation velocity of the piston \hat{V}_p as $U = 5\hat{V}_p/\sqrt{2}$ (see [41] for details), and f is the piston oscillation frequency. In the present case, we have $\text{Re} = 13329$ and $\text{St} = 0.03$, which give a flow lying in the laminar-transitional regime. The flow is fully turbulent in the far field, but laminar in the near field (near the orifice), which will be the region of the jet considered here; see [41] for further details on the experimental facility and the PIV measurement.

The orifice is circular and the resulting near field flow is approximately axi-symmetric, at least in the large scale. The experimental data consists in $K = 1872$ snapshots representing 12 piston oscillation cycles, giving the streamwise and radial velocity components, $u(x_i, r_j, t_k)$ and $v(x_i, r_j, t_k)$, respectively, at $I \times J = 52 \times 68$ grid points in a meridional rectangle (interrogation window), where x and r are the streamwise and radial coordinates, respectively, with origin at the center of the orifice and t is the time variable, with

origin at the beginning of the suction phase. The time variable has been rescaled such that the (nondimensional) oscillating frequencies are measured in terms of the associated Strouhal number defined above, meaning that the piston oscillating period is $T = 2\pi/0.03$. Thus, we have a snapshot tensor (instead of a matrix) and HOSVD must be used instead of standard SVD in the first step of the HODMD method (see [41] for details). Assuming permanent dynamics (zero or very small growth rates) the aim of the iterative HODMD method is to obtain an expansion of the form

$$\mathbf{v}(x, r, t) \approx \sum_{n=1}^N \mathbf{u}_n(x, r) e^{i\omega_n t}, \quad (30)$$

The iterative DMD- d algorithm has been applied to obtain this expansion using two values of the index d , namely, $d = 1$ (standard DMD) and $d = 700$ (strictly higher order DMD), with two tolerance sets, namely,

$$\begin{aligned} \varepsilon_1 &= \varepsilon_2 = 2.4 \cdot 10^{-2} \text{ (low accuracy)}, \\ \varepsilon_1 &= \varepsilon_2 = 10^{-2} \text{ (high accuracy)}, \end{aligned} \quad (31)$$

which correspond to the estimated experimental error and more precise computations, respectively. Using the latter tolerances, below the experimental error, will permit elucidating the ability of the iterative HODMD method to uncover physical phenomena that are masked by the experimental errors in the given data.

Figure 6 shows the amplitude versus frequency (nondimensionalized as the Strouhal number) obtained in the analyses. DMD-1 captures 11 modes, all of them spurious.

On the contrary, DMD-700 captures $N = 19$ and $N = 49$ DMD modes using low and high accuracy, respectively. It is remarkable that the spatial complexity M is much smaller than the spectral complexity, N , since $M = 5$ and $M = 11$ for low and high accuracy, respectively, which justifies the failure of DMD-1. The method shows that the flow is periodic in the near field, with dominant frequency $\text{St} = 0.03$ (piston oscillation frequency). Since the data are real, the DMD modes appear in complex-conjugate pairs, meaning that the retained modes contain the mean flow ($\text{St}=0$) and 9 and 24 nonzero harmonics for low and high accuracy, respectively.

The suction phase (see Figure 5-left) is not quite demanding, since it just shows a saddle point at the axis of the jet. The reconstructions using DMD-700 with low and high accuracies are qualitatively similar to their counterparts for

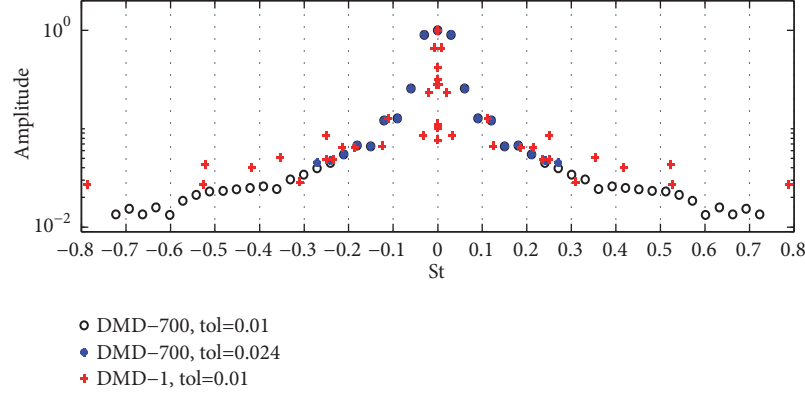


FIGURE 6: Amplitude versus St obtained for low accuracy via DMD-1 (red crosses) and DMD-700 (blue circles) and for high accuracy using DMD-700 (black circles).

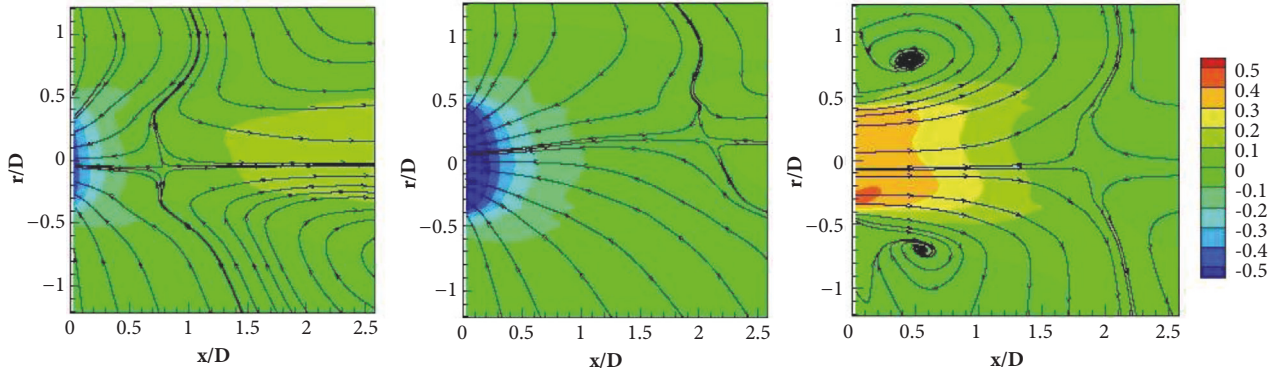


FIGURE 7: Two snapshots in the suction phase, for $t = T/18$ (left plot) and $t = 2T/9$ (middle plot), and a snapshot at the very beginning of the injection phase, for $t = T/2 + T/72$ (right plot).

the original PIV data. The main difference is that the iterative HODMD method gives smoother results with high accuracy than with low accuracy, and both are smoother than the original PIV data. This is an indication of the ability of the method to filter experimental errors, but this issue cannot be confirmed because the actual physical data are not available. Concentrating on the reconstructions with low accuracy, it is seen that the saddle point is created near the orifice at the beginning of this phase and travels downstream to a distance that is approximately equal to $2D$, where it remains steady for most part of the suction phase (Figure 7, left and middle plots). This saddle point is blown downstream at the beginning of the injection phase, where a new saddle point is created near the orifice that travels downstream very fast (Figure 7, right plot) and leaves the near field, in a short timespan of the order of $T/100$. This saddle point must be present for topological reasons, but it had never been seen in studies previous to [41], just because it is quite short living. In fact, it is not present in any of the snapshots used to apply the HODMD method. It must be noted that this saddle point would be present (with some spatial noise) in the experimental snapshots if the sampling frequency was sufficiently large. Thus, the identification of this saddle point illustrates well the advantages of the temporal interpolation that is implicit in the HODMD method.

The injection phase (see Figure 5, right) is more interesting in the present context. Figure 8 shows a comparison of the original data with the reconstructions provided by DMD-700 for low and high accuracy. As can be seen, the reconstructions are much smoother than the original PIV data, as it happened in the suction phase. However, the reconstruction with high accuracy (recall that this is below the experimental error) is qualitatively different, since it shows some small vortices leaving the edge of the cavity that cannot be even guessed in the original PIV data and do not appear in the low accuracy reconstruction because they involve a quite small energy. These small vortices are smooth, which may indicate that they are not artifacts associated with higher order modes resulting from experimental errors. However, this cannot be ascertained since the actual physical dynamics is not available. Therefore, we have conducted some numerical simulations to elucidate this point. The value of the Reynolds number in the experimental data considered above, $Re \sim 13000$, is a quite large value that would need huge numerical resources, even using the computationally efficient solver Nek5000 [54] (an open source spectral element code). Therefore, we have performed computations using the lower Reynolds number $Re=1000$ and the same Strouhal number as in the experimental data considered above, namely, $St=0.03$. The numerical counterpart of the snapshot considered in

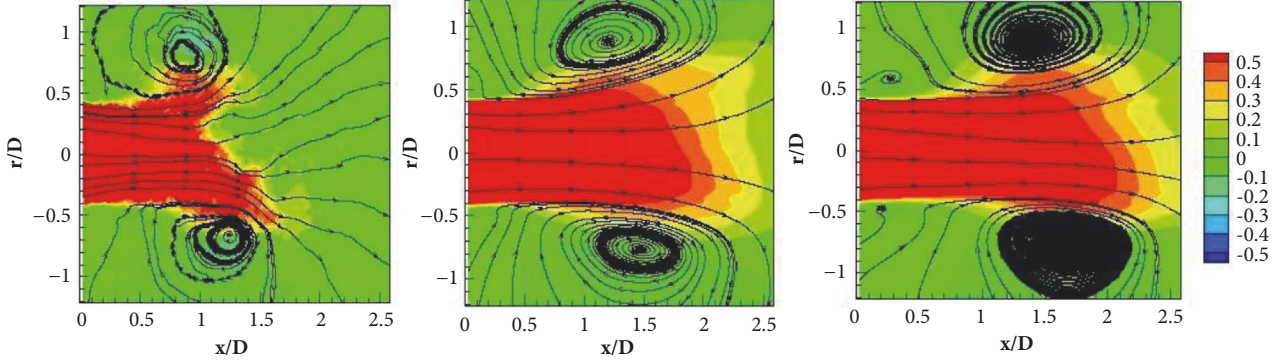


FIGURE 8: Instantaneous pseudo-streamlines and streamwise velocity contours for a representative snapshot ($t = T/9$) in the injection phase, showing the original PIV data (left plot) and the reconstructions using DMD-700 for low (middle plot) and high (right plot) accuracy.

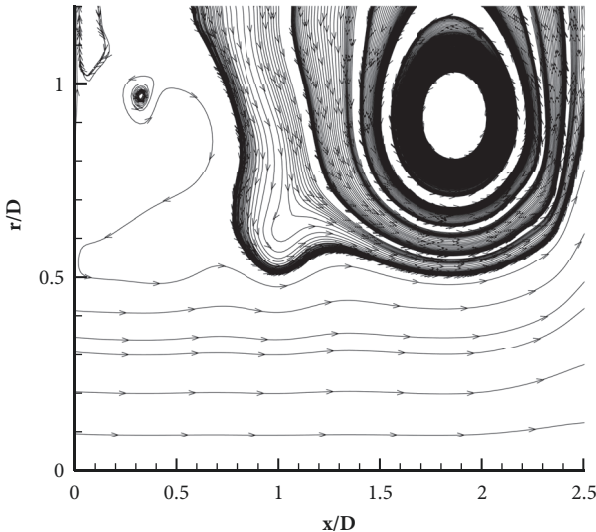


FIGURE 9: Counterpart of the snapshot considered in Figure 5 but as numerically computed for $Re=1000$.

Figure 8 is given in Figure 9, which confirms the presence of the small vortices.

In summary, the results above illustrate well the ability of the iterative HODMD method to both (i) take advantage of temporal interpolation to uncover fast events (such as the saddle point at the beginning of the injection phase) that are not present in the snapshots and (ii) filter experimental errors so well that some small patterns (such as the small vortices in the injection phase) can be identified that were completely masked by the experimental noise. In addition, the analysis above permits constructing a purely data-driven (from experimental data) ROM that reproduces well the periodic behavior of the ZNMF jet and shows a fast online operation.

3.3. Additional Applications. Some additional applications are now briefly quoted.

The HODMD method permits identifying flow instabilities by monitoring those DMD modes whose growth rate

changes sign. On the other hand, as anticipated, retaining only those terms appearing in the DMD expansion (1) that exhibit zero (or very small) growth rate, the final attractor may be obtained from transient data. This latter idea can be used to strongly decrease the CPU time required to compute the final attractor, avoiding continuing the numerical integration until final attractor is reached, which may require an extremely large timespan, specially near bifurcation points. Transient dynamics are usually found in the initial stage of a numerical simulation, where a large number of modes (either physical or spurious) appear simultaneously.

Let us illustrate these two applications by considering the cylinder wake, namely, the wake behind a circular cylinder immersed in a free stream with constant, spatially uniform velocity, which is a basic fluid dynamics problem [55, 56]. This problem depends on a unique nondimensional parameter, the Reynolds number $Re = UD/\nu$, where U is the free stream velocity, D is the cylinder diameter, and ν is the dynamic viscosity of the fluid, assumed to be incompressible. Thus, the nondimensional velocity and pressure obey the continuity and Navier-Stokes equations:

$$\nabla \cdot \mathbf{v} = 0, \quad (32)$$

$$\frac{\partial \mathbf{v}}{\partial t} + (\mathbf{v} \cdot \nabla) \mathbf{v} = -\nabla p + \frac{1}{Re} \Delta \mathbf{v}, \quad (33)$$

which are usually integrated imposing \mathbf{v} is equal to the free stream velocity at the inlet boundary, no-slip boundary conditions at the boundary of the body, appropriate (non-reflecting) boundary conditions at the sides and exit of the computational domain, and periodic boundary conditions in the spanwise direction, with a period L_z . The wake is two-dimensional and steady for small Re , but at $Re \approx 46$ it exhibits a first unsteady instability (Hopf bifurcation [57, 58]) that produces a still two-dimensional but unsteady, periodic von Karman vortex street flow. The flow remains orbitally stable up to $Re \approx 190$, where it suffers a secondary bifurcation (Floquet multiplier = 1) and becomes three-dimensional [59] for spanwise period $L_z > 3D$ (with D the cylinder diameter). The resulting mode is a long-wave, periodic, flow known as *mode A*. For larger values of Re , at $Re=259$, a second periodic short-wave mode appears if $L_z > 1.5D$ that is known as *mode*

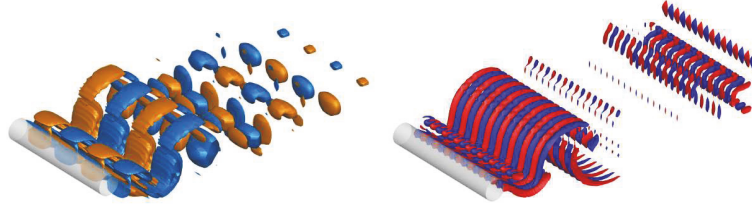


FIGURE 10: Streamwise velocity contours for modes A (left) and B (right) obtained at $Re = 280$, with $L_z = 6.99$.

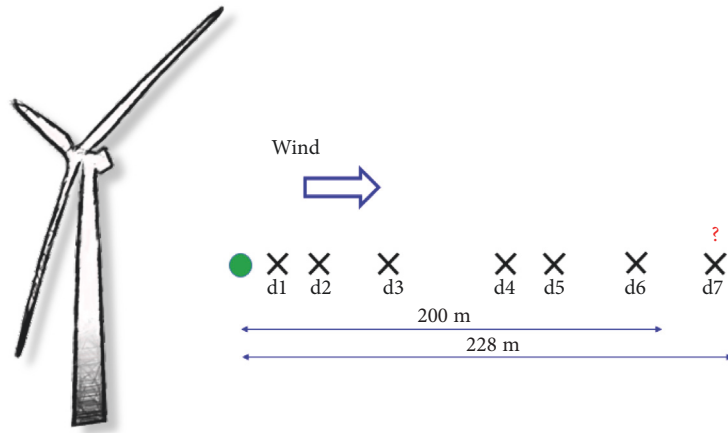


FIGURE 11: Measurements upstream the wind turbine in the LiDAR experimental campaign. Data are available in the six planes that are closer to the wind turbine, while the data on the seventh plane are to be predicted.

B. Modes A and B are illustrated in Figure 10. These modes are usually obtained via Floquet stability analysis of the basic two-dimensional periodic solution [59–61], but they can also be obtained via HODMD applied to the whole dynamics obtained via numerical simulations [62]. It is relevant to note that for higher values of the Reynolds number, at $Re \approx 380$, a new instability takes place that is associated with a pair of complex-conjugate Floquet multipliers that give a family of *quasi-periodic solutions* [61]. These modes were also identified in [62].

As for temporal extrapolation via the HODMD method, this idea has been used [11] precisely in the three-dimensional cylinder wake, with $Re=220$ and $L_z = 4$. The numerical data was obtained using the above-mentioned numerical solver Nek5000 [54]. Temporal HODMD extrapolation divided by five the CPU time required computing the final attractor with a reasonable accuracy; see [11] for further details.

Additional applications involving numerically generated data include the analysis of the turbulent wake of a cross flow wind turbine [63] and an off-shore wind turbine [64], as well as the analysis of wakes interaction [65].

Concerning analyses based on experimental data, a good example, linked to the field of renewable energies, is the postprocess of light detection and ranging (LiDAR) [66, 67] measurements. LiDAR is an experimental method for the remote measurement of the line-of-sight component of wind speed, usually employed in the wind energy industry with different goals, including the maximization of the power generated by the wind turbine. Measurements are made at

a few (say, M) points upstream the wind turbine, based on detection of the Doppler shift for light backscattered from natural aerosols transported by the wind in the atmosphere. LiDAR measurements offer M time-dependent signals that present high noise levels (15 – 20%). Thus, the spatial complexity M is small, making HODMD a suitable tool to analyze the data and detect the dominant frequencies. A great difficulty is that LiDAR experiments only measure at distances between 20 m and 200 m from the measurement device, which is a restriction in certain situations. Figure 11 shows six planes of LiDAR measurements located at distances between 33 m and 201 m upstream the wind turbine. HODMD is used to analyze such data and to predict the wind velocity at a seventh distance (228 m), which is well beyond the LiDAR device measurement range. The idea used in [68] is to extrapolate the spatial modes in the DMD expansion, guessing the data at the seventh distance with relative errors $\sim 2\%$. The computational cost for predicting these measurements is negligible, making it possible to easily update the model in real-time (leading to a fast, purely data-driven ROM).

Additional applications using experimental data where the HODMD method have proved to give good results including nonisothermal flows around square objects in a channel [69] and the analysis of aeroelastic data in aircraft flight tests [70]. The aim in the latter application is to obtain the natural aeroelastic frequencies, and the associated damping rates, of the various aircraft parts (e.g., wings or fuselage) from data obtained at some sensors along the

aircraft when this is subject to various types of impulsive excitation.

4. Spatiotemporal Koopman Decomposition

As seen in the previous sections, HODMD is suited for analyzing complex dynamics and provides accurate signal descriptions in terms of dominant frequencies and DMD modes. Nevertheless, the spatial components of the data analyzed may bring some relevant information that, combined with the temporal information, helps in the analysis and interpretation of the data. The main benefit of this idea, which gives rise to the spatiotemporal Koopman decomposition (STKD) method presented below, is that it further simplifies the spatiotemporal description of complex data in terms of TWs. The STKD method leads to data approximations of the type of (11), which for the sake of clarity is rewritten here as

$$\mathbf{v}(x, y, t) = \sum_{m,n} a_{mn} \mathbf{u}_{mn}(y) e^{(\gamma_m + i\kappa_m)x + (\delta_n + i\omega_n)t}, \quad (34)$$

for $x_1 \leq x \leq x_1 + X$ and $t_1 \leq t \leq t_1 + T$. This expansion can be seen as a linear combination of *monochromatic* TWs, with phase velocities $c_{mn} = -\omega_n/\kappa_m$, which may be organized in various types of more complex standing or propagative patterns [28]. For a given finite accuracy, it is frequent that only some combinations of m and n need to be retained that, moreover, are grouped along straight lines in ω versus κ plane (called the ω - κ diagram below), which may be either horizontal or oblique and correspond to either *standing* or *traveling* patterns, respectively.

Pure TWs are a particular case, in which the number of spatial and temporal modes coincide, the amplitude matrix a_{nm} is diagonal, $\delta_n = \gamma_m = 0$, and $\omega_n = -c\kappa_m$. Then, (34) can be expressed as

$$\mathbf{v}(x - ct, y) \approx \sum_{n=1}^N a_{nn} \mathbf{u}_{nn}(y) e^{i\kappa_m(x-ct)}. \quad (35)$$

In this case, the relevant points in the ω - κ diagram are in a straight line passing through the origin. If $c = 0$, then the pattern is a pure SW. When the points in the ω - κ diagram can be organized in families of horizontal or oblique, parallel straight lines, then the pattern is a modulated SW or TW, respectively. Combinations of these two give more general patterns; see the examples presented below.

In some cases, the dynamics present oscillatory behavior in more than one spatial direction. Concentrating for simplicity in the case in which two spatial directions x and y are involved, the STKD method provides an expansion of the type

$$\mathbf{v}(x, y, z, t) \approx \sum_{m_1, m_2, n} a_{m_1 m_2 n} \mathbf{u}_{m_1 m_2 n}(z) \cdot e^{(\gamma_{m_1}^1 + i\kappa_{m_1}^1)x + (\gamma_{m_2}^2 + i\kappa_{m_2}^2)y + (\delta_n + i\omega_n)t}, \quad (36)$$

which also give TWs. For instance, if the temporal and spatial growth rates are all equal to zero and the wavenumbers and frequencies are such that

$$\begin{aligned} \frac{\omega_n}{\sqrt{(\kappa_{m_1}^1)^2 + (\kappa_{m_2}^2)^2}} &= -c, \\ \kappa_{m_2}^2 &= d\kappa_{m_1}^1, \end{aligned} \quad (37)$$

then pattern (36) represents a pure TW with phase velocity c that propagates in the direction of the lines $dy - x = \text{constant}$. As in the simpler case in which only one spatial direction is involved, pure SWs correspond to the case $c = 0$, and more general patterns are obtained combining these basic patterns. The extension to the case in which the three spatial variables are involved is straight forward.

4.1. The STKD Method. Let us now present the STKD method, considering the discrete counterpart of (34), with the discrete values of x and t defined as $x_j = x_1 + j\Delta x$ and $t_k = t_1 + k\Delta t$, for $j = 1, \dots, J$ and $k = 1, \dots, K$, with $\Delta x = X/J$ and $\Delta t = T/K$; as in the temporal HODMD method, the continuous decomposition is obtained from the discrete decomposition by just allowing x_j and t_k to take continuous values. In addition, for simplicity, we consider a scalar state variable in the strictly one-dimensional case, in which no dependence on the transversal variable y is present. Namely, we substitute (34) by

$$\mathbf{v}(x_j, t_k) = \sum_{m,n} a_{mn} \mathbf{u}_{mn} e^{(\gamma_m + i\kappa_m)x_j + (\delta_n + i\omega_n)t_k}, \quad (38)$$

where the modes \mathbf{u}_{mn} are complex numbers with unit absolute value. The method proceeds in two steps.

Step 1 (dimension reduction). As in HODMD, truncated SVD with a tunable tolerance ϵ_1 (which determines the number of retained SVD modes, M) is applied to the $J \times K$ snapshot matrix (15), but in the present case the reduced spatial and temporal modes are scaled differently. In other words, (17) is replaced by

$$\mathbf{V}_1^K \approx \mathbf{P} \boldsymbol{\Sigma} \mathbf{Q}^\top \equiv \left(\widehat{\mathbf{X}}_1^J \right)^\top \widehat{\mathbf{T}}_1^K, \quad (39)$$

where $M \times J$ and $M \times K$ matrices $\widehat{\mathbf{X}}_1^J$ and $\widehat{\mathbf{T}}_1^K$ are defined as

$$\begin{aligned} \widehat{\mathbf{X}}_1^J &= \sqrt{\boldsymbol{\Sigma}} \mathbf{P}^\top, \\ \widehat{\mathbf{T}}_1^K &= \sqrt{\boldsymbol{\Sigma}} \mathbf{Q}^\top. \end{aligned} \quad (40)$$

These matrices are called the *reduced spatial and temporal snapshot matrices*, respectively, and their columns, $\widehat{\mathbf{x}}_j$ and $\widehat{\mathbf{t}}_k$, the *reduced spatial and temporal snapshots*, respectively. Comparison between (40) and (17) shows that while the SVD singular values were used in the temporal HODMD method to scale the reduced temporal snapshots, they are equidistributed now to rescale the reduced spatial and temporal snapshots, which are both scaled with the square root of the singular values.

Step 2 (computation of the STKD expansion). The higher DMD-d algorithm described in Section 2 is applied to the reduced spatial and temporal snapshots, using appropriate indexes d^x and d^t , respectively, which leads to

$$\hat{\mathbf{x}}_j \simeq \sum_{m=1}^M \hat{a}_m^x \hat{\mathbf{q}}_m^x e^{(\gamma_m + i\kappa_m)x_j}, \quad \text{for } j = 1, \dots, J, \quad (41)$$

$$\hat{\mathbf{t}}_k \simeq \sum_{n=1}^N \hat{a}_n^t \hat{\mathbf{q}}_n^t e^{(\delta_n + i\omega_n)t_k} \quad \text{for } k = 1, \dots, K. \quad (42)$$

The numbers of retained modes, M and N , are the *spectral spatial and temporal complexities*, respectively, and are selected in terms of the spatial and temporal amplitudes, \hat{a}_m^x and \hat{a}_n^t , respectively, as we did in Section 2. Namely, M and N are the smallest values of the indexes m and n such that

$$\begin{aligned} \frac{\hat{a}_{M+1}^x}{\hat{a}_1^x} &< \varepsilon_2, \\ \frac{\hat{a}_{N+1}^t}{\hat{a}_1^t} &< \varepsilon_2. \end{aligned} \quad (43)$$

for some tunable tolerance ε_2 .

Now, substituting (41)-(42) into the columns of the reduced snapshot matrices $\hat{\mathbf{X}}_1^J$ and $\hat{\mathbf{T}}_1^K$ appearing in (39) yields the STKD expansion (38), with

$$\begin{aligned} a_{mn} &= |\hat{q}_{mn}| > 0, \\ q_{mn} &= \frac{\hat{q}_{mn}}{|\hat{q}_{mn}|}, \end{aligned} \quad (44)$$

where

$$\hat{q}_{mn} = \hat{a}_m^x \hat{a}_n^t (\hat{\mathbf{q}}_m^x)^\top \hat{\mathbf{q}}_n^t. \quad (45)$$

Note that the modes q_{mn} are complex numbers exhibiting unit absolute value, as required, and that the resulting expansion (38) exhibits $M \times N$ spatiotemporal modes. However, this number of modes can be decreased by eliminating those modes such that

$$a_{mn} < \varepsilon_2, \quad (46)$$

where the threshold ε_2 is tunable.

The method described above can be called a *parallel method* because the spatial and temporal variables, x and t , are treated in the same way. The extension of the method to the case in which more than one spatial variable is involved (see, e.g., (34) and (36)) is straight forward, except that the snapshot matrix becomes a snapshot tensor and HOSVD needs to be used instead of SVD in Step 1 (as in Section 3.2). For the sake of brevity, we do not describe this extension here; see [28] for a detailed development and illustration of this extension.

Instead of the parallel method described above, a simpler but less consistent *sequential method* may be used to obtain

the discrete STKD expansion (38) as follows. First, the temporal DMD-d algorithm described in Section 2, with an appropriate index d^t , is applied to the snapshot matrix, which leads to

$$v(x_j, t_k) \simeq \sum_{n=1}^N a_n^t u_{nj}^t e^{(\delta_n + i\omega_n)t_k}. \quad (47)$$

As a second step, we apply the spatial DMD-d algorithm, with an appropriate index d^x , to the $N \times J$ snapshot matrix \mathbf{W}_1^J whose (n, j) element is $a_n^t u_{nj}^t$, which leads to

$$a_n^x u_{nj} \simeq \sum_{m=1}^M a_m^x u_{mn}^x e^{(\gamma_m + i\kappa_m)x_j}. \quad (48)$$

Substituting this into (47) and setting

$$\begin{aligned} a_{mn} &= |a_m^x u_{mn}^x|, \\ u_{mn} &= \frac{a_m^x u_{mn}^x}{|a_m^x u_{mn}^x|} \end{aligned} \quad (49)$$

yields the discrete expansion (38), as required. However, as in the parallel method, the number of terms in this expansion is $M \times N$, which can be decreased by ignoring those modes that satisfy (46).

Two remarks about the sequential method are now in order:

- (i) The order in which the variables x and t are treated above can be interchanged, which generally gives slightly different results.
- (ii) As with the parallel method, when more than one spatial variable is present, the snapshot matrix becomes a snapshot tensor and standard SVD must be replaced by HOSVD in the application of the HODMD method.

Because the parallel method is more consistent, specially when treating more than one spatial variable, it will be this method that will be used in the remainder of this section, unless otherwise stated.

As with the HODMD, the STKD method can be used to analyze experimental data. The noisy artifacts that may cover the actual physical data can be cleaned using the proper tolerances and applying the method iteratively (as in the example presented in Section 3.2). Similarly, the STKD method is suitable for analyzing transient dynamics (as in the example shown in Section 3.3).

4.2. Illustration of the STKD Method in a Toy Model. Let us now apply these two methods in the following toy model, already considered in [29], defined as

$$\begin{aligned} u(x, t) &= (0.5 + \sin x) \\ &\cdot [2 \cos(\tilde{\kappa}_1 x - \tilde{\omega}_1 t) + 0.5 \cos(\tilde{\kappa}_2 x - \tilde{\omega}_2 t)], \end{aligned} \quad (50)$$

with $\tilde{\kappa}_1 = 2$, $\tilde{\kappa}_2 = 10$, $\tilde{\omega}_1 = 2\pi/45$, and $\tilde{\omega}_2 = \sqrt{10}$. It is a simple (but demanding because $\tilde{\omega}_1$ and $\tilde{\omega}_2$ are disparate from each

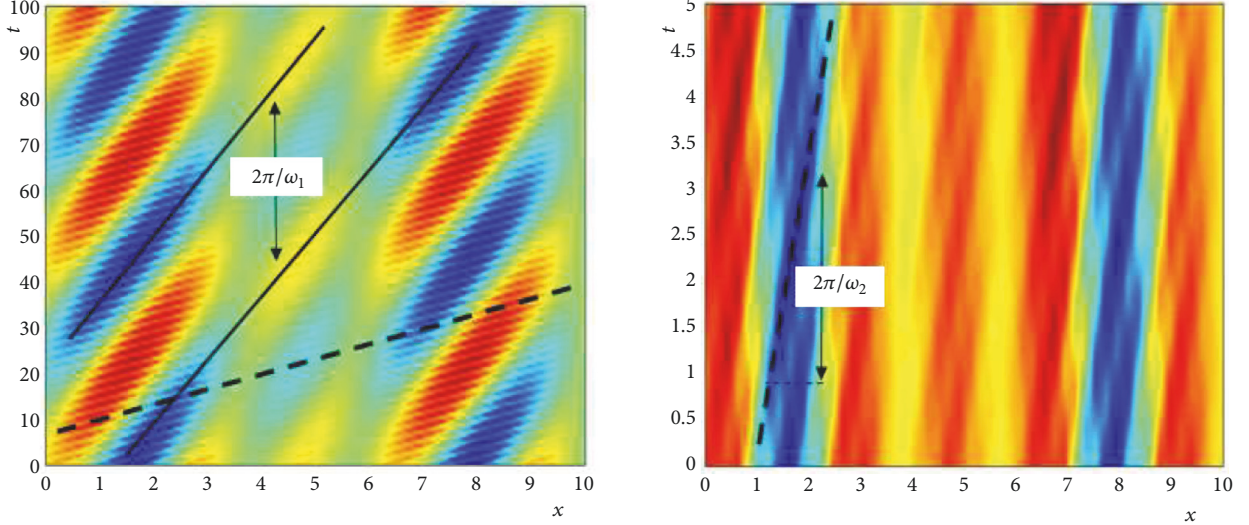


FIGURE 12: Color map of the toy model (50) (left plot) and its restriction to the sampled spatiotemporal square where the STKD method is applied (right plot).

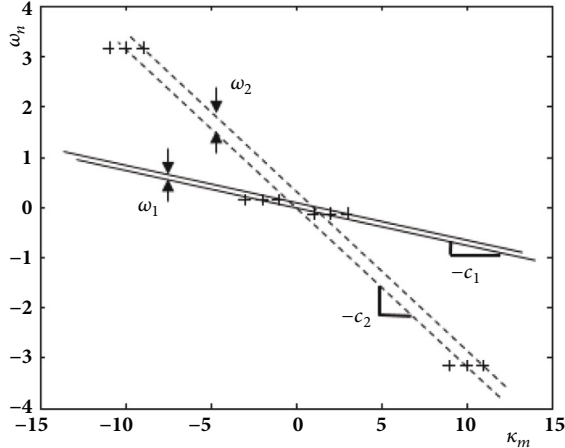


FIGURE 13: \$\omega - \kappa\$ diagram of the toy model (50).

other; see Figure 12-left) model that can be cast into the form (34), with \$\nu_m = \delta_n = 0\$, involving 12 wavenumbers, namely, \$\pm\tilde{\kappa}_1, \pm\tilde{\kappa}_2, \pm(\tilde{\kappa}_1 \pm 1), \pm(\tilde{\kappa}_2 \pm 1)\$, and 4 frequencies, namely, \$\pm\tilde{\omega}_1\$ and \$\pm\tilde{\omega}_2\$. Thus the spectral spatial and temporal complexities are \$M = 12\$ and \$N = 4\$, respectively. The pattern is temporally quasi-periodic because \$\tilde{\omega}_1\$ and \$\tilde{\omega}_2\$ are incommensurable, but spatially periodic, with a period equal to \$2\pi\$.

The STKD method is applied in the sampled square \$0 \leq x \leq 10, 0 \leq t \leq 5\$ (see Figure 12, right), where \$x\$ and \$t\$ are discretized using 50 and 25 points, respectively. The tunable parameters of the method are \$\varepsilon_1 = 10^{-8}, \varepsilon_2 = 10^{-7}, d^x = 1\$, and \$d^t = 10\$. The obtained \$\omega-\kappa\$ diagram is given in Figure 13, which shows that the pattern is a modulated TW, obtained as a linear superposition of two pure TWs, whose phase velocities are \$c_1 = \omega_1/\kappa_1 = \pi/45\$ and \$c_2 = \omega_2/\kappa_2 = 1/\sqrt{10}\$. The method provides the involved 12 wavenumbers and 4 frequencies with zero machine accuracy, while the

RRMS error (see (16)) of the reconstruction is \$\sim 10^{-14}\$. It is remarkable that these extremely good results are obtained using a sampled spatial interval that is somewhat larger to the spatial period, but a temporal sampled interval that is much smaller than the largest temporal period, which is \$2\pi/\tilde{\omega}_1 = 45\$. Also note that the extrapolation from the sampled time interval \$0 \leq t \leq 5\$ (Figure 12, right) to the larger time interval \$0 \leq t \leq 100\$ (Figure 12, left) still produces a good reconstruction, whose RRMS error, as defined in (16), is \$\sim 10^{-14}\$.

The sequential method has also been applied to analyze this toy model, obtaining results that are similar to those described above.

5. Applications of STKD

Let us now illustrate in some applications the ability of the STKD method to uncover the spatiotemporal structure of complex dynamics. Among these applications, we consider the CGLE (already analyzed with the temporal HODMD method in Section 3.1) and the dynamics of the thermal convection in a rotating spherical shell subject to gravitational force.

5.1. Application of the STKD Method to the CGLE. For the CGLE, the STKD counterpart of (27) is

$$A(x, t) = e^{i\omega_0 t} \sum_{mn} a_{mn} u_{mn} e^{i(\kappa_m x + \omega_n t)}, \quad (51)$$

where the modes \$u_{mn}\$ are now unit complex numbers. Concentrating on the two cases analyzed in Section 3.1 and Figures 3 and 4, we use the same snapshots and tunable parameters used in Section 3.1, including the index \$d^t\$, which is set as being equal to the index \$d\$ used in Section 3.1. The index \$d^x\$, instead, is set as \$d^x = 1\$. In both cases, the RRMS reconstruction errors, as defined in (16), are comparable to

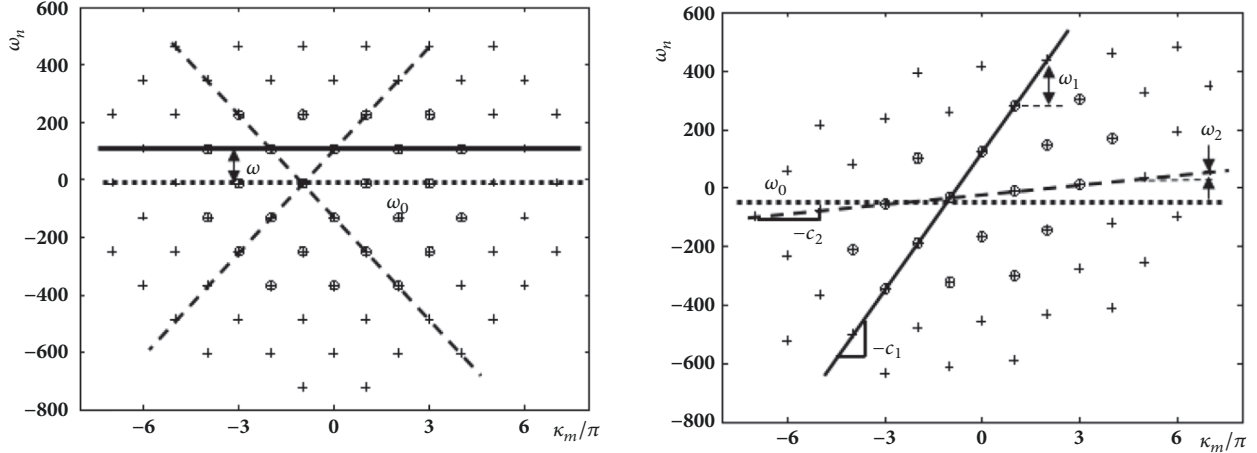


FIGURE 14: ω - κ diagrams resulting from the STKD method applied to the CGLE for the cases considered in Figure 3 (left plot) and Figure 4 (right plot). As in Figure 3, left, and Figure 4, left, crosses and circles label results obtained with high and low accuracies, respectively.

their counterparts obtained in Section 3.1 using the temporal HODMD method, retaining 25 and 71 spatiotemporal modes for low and high accuracy, respectively, in the case considered in Figure 3 and 17 and 49 modes for low and high accuracy, respectively, in the case considered in Figure 4. The ω - κ diagrams for these two cases are given in Figure 14. The left plot in this figure shows that points can be conformed in either horizontal or oblique straight lines, which clearly indicates that the pattern can be considered as either a modulated SW or a modulated TW, consistent with what is clearly seen in Figure 3. As anticipated in Section 3.1, the value of ω_0 in the expansion (51) equals 11.6, while the frequencies ω_n appearing in the expansion in the right hand side of (51) are positive and negative harmonics of the fundamental frequency $\omega_1 = 118.7$, which is associated with the wavenumber $\kappa_1 = \pi$. Thus, this pattern is slowly modulated (because ω_0 is small compared to ω_1) and when it is seen as a TW, the phase velocity is $c = \pm\omega_1/\kappa_1 = \pm37.8$.

Concerning the right plot in Figure 14, the points in this plot are conformed in the indicated oblique straight lines, which means that the pattern is a modulated TW. As in Section 3.1, the frequency ω_0 appearing in (51) equals -21.2, while the various frequencies appearing in the expansion in the right hand side of this equations are all combinations of the fundamental frequencies $\omega_1 = 156.6$ and $\omega_2 = 22.2$, whose associated wavenumbers are $\kappa_1 = \pi$ and $\kappa_2 = 2\pi$, respectively; the associated phase velocities are $c_1 = -\omega_1/\kappa_1 = -49.8$ and $c_2 = -\omega_2/\kappa_2 = -3.53$, which are indicated in Figures 3 and 4, middle and right plots.

In summary, the STKD method computes quite well the frequencies and wavenumbers involved in SWs and TWs for the CGLE and permits straightforward identification of the associated phase velocities.

5.2. STKD in a Three-Dimensional Spherical Shell with Radial Thermal Convection, Subject to Radial Gravity. Let us consider the three-dimensional thermal convection in a rotating spherical shell, heated from the inside, subject to a radial

gravitational force. This problem is relevant in geophysical and astrophysical fluid dynamics [71], in connection with the transport of mass and energy in the upper atmospheres of stars and giant planets, where it is specially interesting the identification of periodic and quasi-periodic rotating waves promoted by convective instabilities.

The continuity, momentum, and energy equations governing the dynamics of the flow, using the Boussinesq approximation in a rotating (with angular velocity Ω) frame linked to the spherical shell, are

$$\nabla \cdot \mathbf{v}, \quad (52)$$

$$\partial_t \mathbf{v} + (\mathbf{v} \cdot \nabla) \mathbf{v} + 2E^{-1} \mathbf{k} \times \mathbf{v} = -\nabla \Pi + \nabla^2 \mathbf{v} + \Theta \mathbf{r}, \quad (53)$$

$$\sigma (\partial_t \Theta + \mathbf{v} \cdot \nabla \Theta) = \nabla^2 \Theta + R\eta (1-\eta)^{-2} r^{-3} \mathbf{r} \cdot \mathbf{v}. \quad (54)$$

Here, \mathbf{v} , Π , and Θ are the velocity vector, the pressure, and the perturbation of the temperature from the quiescent purely convective state, respectively, $\mathbf{r} = (x, y, z)$ is the position vector referred to a Cartesian coordinate system, with the origin at the center of the sphere and the z axis along the axis of rotation, $r = |\mathbf{r}|$, and \mathbf{k} is the unit vector along the z axis. The boundary conditions are homogeneous Dirichlet for both the velocity and temperature at the inner and outer spheres.

The problem depends on three *nondimensional parameters*, the *Prandtl number* $\sigma = \nu/\kappa$ (where ν and κ are the kinematic viscosity and thermal conductivity, respectively), the *Eckman number* $E = \nu/(\Omega d^2)$ (where $d = r_o^* - r_i^*$ is the radial gap between the spheres), the *Rayleigh number* $R = \gamma\alpha\Delta T d^4/(\nu\kappa)$ (where α is the thermal expansion coefficient, γr_i^* is the imposed radial gravity, and ΔT is increment in temperature), and the *inner to outer radii ratio* $\eta = r_i^*/r_o^*$. This problem is invariant under the symmetry group $SO(2) \times \mathbb{Z}_2$, generated by rotations about the z axis and up-down reflection on the equatorial plane. Invariance under rotation is essential to obtain TWs (which are rotating waves along the azimuthal direction in the present context), most of which are

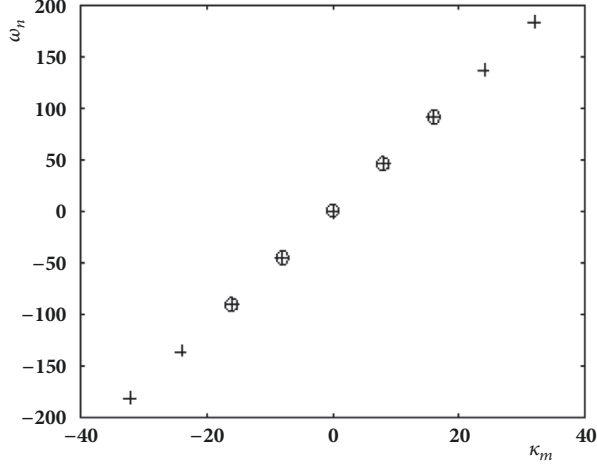


FIGURE 15: The ω - κ diagram (with circles and crosses indicating low and high accuracy) for the attractor at $R = 8 \cdot 10^5$.

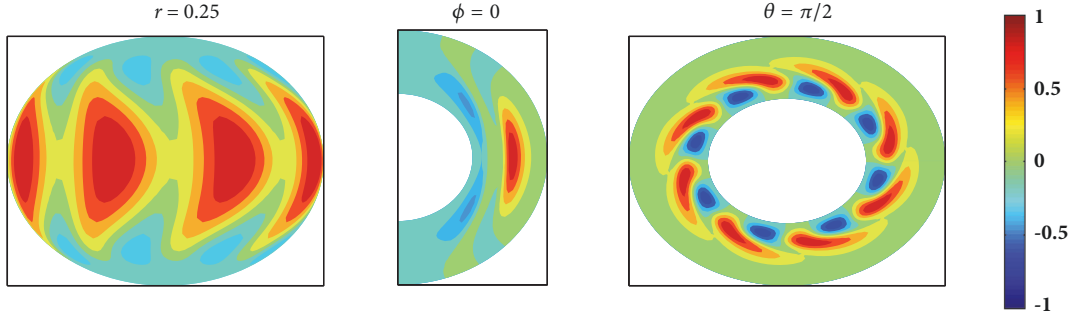


FIGURE 16: A snapshot showing the contour levels of Θ at the indicated surfaces for $R = 8 \cdot 10^5$.

also (instantaneously) invariant under the up/down reflection symmetry.

The computational domain is composed by 25, 128, and 32 grid points in the radial, colatitudinal, and azimuthal directions, respectively. The *numerical solver* used to solve this problem is described in [72–75], where the problem is reformulated by taking the curl of the momentum equation (which eliminates the pressure) and writing the solenoidal velocity field (which eliminates the continuity equation) as

$$\mathbf{v} = \nabla \times (\Psi \mathbf{r}) + \nabla \times \nabla \times (\Phi \mathbf{r}), \quad (55)$$

where Ψ and Φ are the *toroidal and poloidal scalar potentials*, respectively, first introduced by Chandrasekhar [76]. The numerical data used in the analysis below have been provided to us by Professors Marta Net and Joan Sánchez. These data correspond to $E = 10^{-4}$, $\eta = 0.35$, $\sigma = 0.1$, and two values of the Rayleigh number, namely, $R = 8 \cdot 10^5$ and $R = 1.1 \cdot 10^6$. In both cases, the STKD method is applied to the temperature field, which gives the expansion

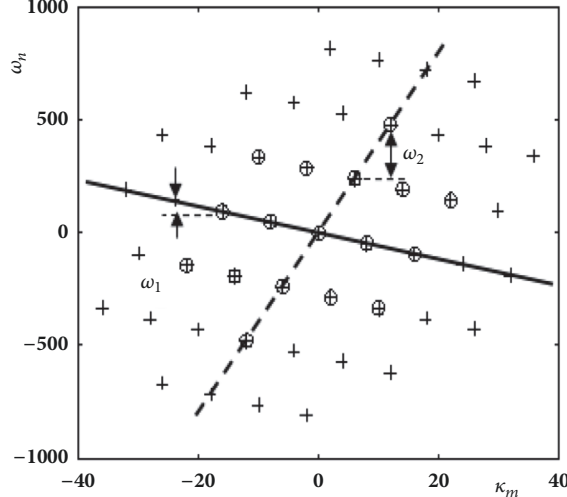
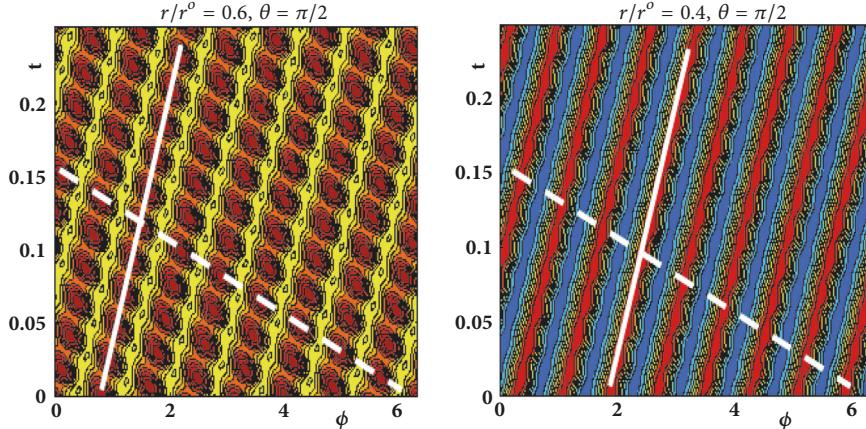
$$\Theta(r_{j_1}, \theta_{j_2}, \phi, t) \approx \sum_{m,n=1}^{M,N} a_{mn} \Theta_{mnj_1j_2} e^{i(k_m \phi + \omega_n t)}, \quad (56)$$

where r_{j_1} and θ_{j_2} denote the mesh points in the radial and colatitudinal directions, respectively, and ϕ denotes the

azimuthal coordinate. As in the previous applications of the STKD method, two sets of values of the tunable parameters are considered, namely, $(\epsilon_1, \epsilon_2) = (10^{-4}, 5 \cdot 10^{-3})$ and $(10^{-5}, 5 \cdot 10^{-4})$, which will be referred to as low and high accuracy, respectively. The index d may be selected as $d = 1$ for both the spatial and temporal applications of the HODMD method that are needed in the second step of the STKD method.

For $R = 8 \cdot 10^5$, the STKD method is applied considering 100 equispaced snapshots in a time interval of length 0.3, selected after sufficiently large timespan to eliminate transient behavior. The RRMS reconstruction error, as defined in (16), is $1.6 \cdot 10^{-3}$ and $1.5 \cdot 10^{-5}$ for low and high accuracies, respectively, retaining 5 and 9 spatiotemporal modes, respectively. The ω - κ diagram is as given in Figure 15, which shows that for both low and high accuracy; the relevant points (whose frequencies and wavenumbers are multiples of $\omega_1 = 45.5$ and $\kappa_1 = 8$, respectively) are in a straight line passing through the origin. As explained in Section 4, this means that the pattern is a periodic, pure TW; namely, it is steady in a rotating frame with phase speed, $c = -\omega_1/\kappa_1 = -5.69$. Such a steady solution is considered in Figure 16, where the fundamental wavenumber $\kappa_1 = 8$ is clearly seen in the equatorial section $\phi = \pi/2$.

Concerning the case $R = 1.1 \cdot 10^6$, in which the dynamics are more complex than in the former case, the STKD method is applied considering 500 equispaced snapshots in a time

FIGURE 17: Counterpart of Figure 15 $R = 1.1 \cdot 10^6$.FIGURE 18: The quasi-periodic TW for $R = 1.1 \cdot 10^6$: color maps of Θ along the azimuthal coordinate at the indicated equatorial circles.

interval of length 1.4, again selected after sufficiently large timespan to eliminate transient behavior. Now, the RRMS reconstruction error, as defined in (16), is $8 \cdot 10^{-3}$ and $1.4 \cdot 10^{-4}$ for low and high accuracies, respectively, retaining 17 and 47 spatiotemporal modes, respectively. The $\omega\text{-}\kappa$ diagram is as given in Figure 17, where it can be seen that the relevant points are aligned along oblique straight lines. The fundamental frequencies and wavenumbers are $(\omega_1, \kappa_1) = (47.6, 8)$ and $(-239.8, 6)$, while the remaining points are linear combinations (with integer coefficients) of these. Thus, the pattern is a modulated TW, which is periodic in a frame moving with either of the phase velocities $c_1 = \omega_1/\kappa_1 = -5.95$ or $c_2 = \omega_2/\kappa_2 = 40$.

Since the counterpart of the space-time diagrams presented for the CGLE in Section 3.1 would lead to four-dimensional plots that are not possible in the present case, the character of the pattern as a modulated TW is illustrated in Figure 18 considering the restricted space-time diagrams (along the azimuthal coordinate) in two equatorial circles. As can be seen in these plots, the modulated TW character (with the already identified phase velocities, indicated here with straight lines) of the pattern is clearly seen.

5.3. Additional Applications. The STKD method has already been used in the analysis of TWs appearing in the following:

- (i) Off-shore wind turbines [64], whose structure is of great technological interest
- (ii) The three-dimensional cylinder wake [77], which permits identifying well the TWs associated with the already mentioned periodic modes A and B, and also with some quasi-periodic modes. These modes play a fundamental role in the associated dynamics [61]

Additional ongoing applications include the following:

- (i) Interacting wakes of bluff bodies, which generally gives complex quasi-periodic phenomena, including at least the frequencies and wavenumbers associated with the individual wakes
- (ii) Several turbomachinery configurations
- (iii) The reconstruction the 3D flow from various (PIV) 2D measurements, taking advantage of the fact that if the 3D flow is given by (34), then the whole unsteady 3D flow field may be reconstructed if the (steady) 2D

- modes $u_{mn}(y)$ are available. These can be computed by fitting with unsteady 2D measurements. Note that this is a demanding application of great scientific and technological interest
- (iv) The identification of the large scale dynamics in fully turbulent flows from either experimental (PIV) or numerical data resulting from direct numerical simulation. Again, this is a demanding application of great scientific interest

6. Conclusions

A review has been presented on the purely data-driven HODMD and STKD methods and their multiple applications. These methods decompose either temporal or spatiotemporal experimental or numerical signals as a combination of modes. In particular, HODMD is an extension of standard DMD that has general validity, namely it provides good results (identifying the relevant temporal growth rates and frequencies) in cases in which standard DMD fails. STKD also computes the relevant spatial growth rates and wavenumbers, and provides $\omega - \kappa$ diagrams that permit identifying TWs or SWs in the given data. These methods allow for two main tasks:

- (i) Uncovering the physics underlying the given data. In particular, in the case of experimental data, these methods are able to filter noise quite efficiently and extract patterns that were completely masked by experimental noise.
- (ii) Constructing ROMs whose online operation is very fast. This is because the HODMD and STKD reconstructions involve semianalytic descriptions that only require a limited amount of operations.

The HODMD and STKD methods have been illustrated in various applications of basic scientific interest, including the CGLE, the ZNMF jet, the thermal convection in a spherical rotating shell, and the wake of a circular cylinder. Several, more engineering oriented applications dealing with, e.g., aircraft flight tests and wind turbine problems, have also been considered.

Conflicts of Interest

The authors declare that they have no conflicts of interest.

Acknowledgments

This work was supported by the Spanish Ministry of Economy and Competitiveness, under Grant TRA2016-75075-R.

References

- [1] W. H. Press, B. P. Flannery, S. A. Teukolsky, and W. T. Vetterling, *Numerical Recipes in C: The Art of Scientific Computing*, Cambridge University Press, Cambridge, UK, 2nd edition, 1988.
- [2] J. Laskar, "Frequency analysis of a dynamical system," *Celestial Mechanics & Dynamical Astronomy*, vol. 56, no. 1-2, pp. 191-196, 1993.
- [3] J. Laskar, "Frequency analysis for multi-dimensional systems. Global dynamics and diffusion," *Physica D: Nonlinear Phenomena*, vol. 67, no. 1-3, pp. 257-281, 1993.
- [4] P. J. Schmid and J. L. Sesterhenn, "Dynamic mode decomposition of numerical and experimental data," in *Proceedings of the Bulletin of the American Physical Society 61st APS meeting, San Antonio*, p. 208, 2008.
- [5] C. W. Rowley, I. Mezic', S. Bagheri, P. Schlatter, and D. S. Henningson, "Spectral analysis of nonlinear flows," *Journal of Fluid Mechanics*, vol. 641, pp. 115-127, 2009.
- [6] P. J. Schmid, "Dynamic mode decomposition of numerical and experimental data," *Journal of Fluid Mechanics*, vol. 656, pp. 5-28, 2010.
- [7] J. H. Tu, C. W. Rowley, D. . Luchtenburg, S. L. Brunton, and J. N. Kutz, "On dynamic mode decomposition: theory and applications," *Journal of Computational Dynamics*, vol. 1, no. 2, pp. 391-421, 2014.
- [8] S. Le Clainche and J. M. Vega, "Higher order dynamic mode decomposition," *SIAM Journal on Applied Dynamical Systems*, vol. 16, no. 2, pp. 882-925, 2017.
- [9] E. N. Lorenz, "Deterministic nonperiodic flow," *Journal of the Atmospheric Sciences*, vol. 20, pp. 130-141, 1963.
- [10] R. Temam, "Inertial manifolds," *The Mathematical Intelligencer*, vol. 12, no. 4, pp. 68-74, 1990.
- [11] S. Le Clainche and J. M. Vega, "Higher order dynamic mode decomposition to identify and extrapolate flow patterns," *Physics of Fluids*, vol. 29, Article ID 084102, 2017.
- [12] T. Sauer, J. A. Yorke, and M. Casdagli, "Embedology," *Journal of Statistical Physics*, vol. 65, no. 3-4, pp. 579-616, 1991.
- [13] F. Takens, "Detecting strange attractors in turbulence," in *Dynamical systems and Turbulence*, D. A. Rand and L. S. Young, Eds., vol. 898 of *Lecture Note in Mathematics*, pp. 366-381, Springer, Berlin, Germany, 1981.
- [14] N. H. Packard, J. D. Farmer, and R. S. Shaw, "Geometry from a time series," *Physical Review Letters*, vol. 45, pp. 712-716, 1980.
- [15] S. L. Brunton, B. W. Brunton, J. L. Proctor, E. Kaiser, and J. Nathan Kutz, "Chaos as an intermittently forced linear system," *Nature Communications*, vol. 8, no. 1, 2017.
- [16] J.-N. Juang and R. S. Pappa, "An eigenvalue realization algorithm for modal parameter identification and model reduction," *Journal of Guidance, Control, and Dynamics*, vol. 8, no. 5, pp. 620-627, 1985.
- [17] D. S. Broomhead and R. Jones, "Time-series analysis," *Proceedings of the Royal Society A Mathematical, Physical and Engineering Sciences*, vol. 423, no. 1864, pp. 103-121, 1989.
- [18] D. Giannakis and A. J. Majda, "Nonlinear Laplacian spectral analysis for time series with intermittency and low-frequency variability," *Proceedings of the National Academy of Sciences of the United States of America*, vol. 109, no. 7, pp. 2222-2227, 2012.
- [19] K. K. Chen, J. H. Tu, and C. W. Rowley, "Variants of dynamic mode decomposition: boundary condition, Koopman, and Fourier analyses," *Journal of Nonlinear Science*, vol. 22, no. 6, pp. 887-915, 2012.
- [20] G. H. Golub and R. J. LeVeque, "Extensions and uses of the variable projection algorithm for solving nonlinear least squares problems," vol. 3 of *ARO Rep. 79*, pp. 1-12, U. S. Army Res. Office, Research Triangle Park, N.C..
- [21] T. Askham and J. N. Kutz, "Variable projection methods for an optimized dynamic mode decomposition," *SIAM Journal on Applied Dynamical Systems*, vol. 17, no. 1, pp. 380-416, 2018.

- [22] M. R. Jovanović, P. J. Schmid, and J. W. Nichols, "Sparsity-promoting dynamic mode decomposition," *Physics of Fluids*, vol. 26, no. 2, p. 024103, 2014.
- [23] M. O. Williams, I. G. Kevrekidis, and C. W. Rowley, "A data-driven approximation of the Koopman operator: extending dynamic mode decomposition," *Journal of Nonlinear Science*, vol. 25, no. 6, pp. 1307–1346, 2015.
- [24] M. S. Hemati, C. W. Rowley, E. A. Deem, and L. N. Cattafesta, "De-biasing the dynamic mode decomposition for applied Koopman spectral analysis of noisy datasets," *Theoretical and Computational Fluid Dynamics*, vol. 31, no. 4, pp. 349–368, 2017.
- [25] S. T. M. Dawson, M. S. Hemati, M. O. Williams, and C. W. Rowley, "Characterizing and correcting for the effect of sensor noise in the dynamic mode decomposition," *Experiments in Fluids*, vol. 57, no. 3, 2016.
- [26] N. Takeishi, Y. Kawahara, Y. Tabei, and T. Yairi, "Bayesian dynamic mode decomposition," in *Proceedings of the 26th International Joint Conference on Artificial Intelligence, IJCAI 2017*, pp. 2814–2821, Australia, August 2017.
- [27] C. Dicle, H. Mansour, D. Tian, M. Benosman, and A. Vetro, "Robust low rank dynamic mode decomposition for compressed domain crowd and traffic flow analysis," in *Proceedings of the 2016 IEEE International Conference on Multimedia and Expo, ICME 2016*, USA, July 2016.
- [28] S. Le Clainche and J. M. Vega, "Spatio-temporal Koopman decomposition," *Journal of Nonlinear Science*, vol. 28, no. 5, pp. 1793–1842, 2018.
- [29] D. Giannakis, J. Slawinska, and Z. Zhao, "Spatiotemporal feature extraction with data-driven Koopman operators," in *Proceedings of the in JMLR: Workshop and Conference*, vol. 44, pp. 103–115, 2015.
- [30] D. Giannakis, A. Ourmazd, J. Slawinska, and Z. Zhao, *Spatiotemporal pattern extraction by spectral analysis of vector-valued observables*, 2017, arXiv preprint 1711.02798.
- [31] A. S. Sharma, I. Mezić, and B. J. McKeon, "Correspondence between Koopman mode decomposition, resolvent mode decomposition, and invariant solutions of the Navier-Stokes equations," *Physical Review Fluids*, vol. 1, no. 3, 2016.
- [32] B. Koopman, "Hamiltonian systems and transformations in Hilbert space," *Proceedings of the National Academy of Sciences of the United States of America*, vol. 17, pp. 315–318, 1931.
- [33] I. Mezic, "Analysis of fluid flows via spectral properties of the Koopman operator," *Annual Review of Fluid Mechanics*, vol. 45, pp. 357–378, 2013.
- [34] M. C. Cross and P. C. Hohenberg, "Pattern formulation outside of equilibrium," *Reviews of Modern Physics*, vol. 65, pp. 851–1112, 1993.
- [35] M. Haragus and G. Iooss, *Local bifurcations, center manifolds, and normal forms in infinite-dimensional dynamical systems*, Universitext, Springer-Verlag London, Ltd., London; EDP Sciences, Les Ulis, 2011.
- [36] C. Gao, W. Zhang, J. Kou, Y. Liu, and Z. Ye, "Active control of transonic buffet flow," *Journal of Fluid Mechanics*, vol. 824, pp. 312–351, 2017.
- [37] K. H. Park, S. O. Jun, S. M. Baek, M. H. Cho, K. J. Yee, and D. H. Lee, "Reduced-order model with an artificial neural network for aerostructural design optimization," *Journal of Aircraft*, vol. 50, no. 4, pp. 1106–1116, 2013.
- [38] G. H. Golub and C. F. van Loan, *Matrix Computations*, The Johns Hopkins University Press, Baltimore, Md, USA, 3rd edition, 1996.
- [39] G. W. Stewart, "Error and perturbation bounds for subspaces associated with certain eigenvalue problems," *SIAM Review*, vol. 15, pp. 727–764, 1973.
- [40] <https://github.com/LeClaincheVega/HODMD>.
- [41] S. Le Clainche, J. M. Vega, and J. Soria, "Higher order dynamic mode decomposition of noisy experimental data: The flow structure of a zero-net-mass-flux jet," *Experimental Thermal and Fluid Science*, vol. 88, pp. 336–353, 2017.
- [42] T. G. Kolda and B. W. Bader, "Tensor decompositions and applications," *SIAM Review*, vol. 51, no. 3, pp. 455–500, 2009.
- [43] L. R. Tucker, "Some mathematical notes on three-mode factor analysis," *Psychometrika*, vol. 31, no. 3, pp. 279–311, 1966.
- [44] I. S. Aranson and L. Kramer, "The world of the complex Ginzburg-Landau equation," *Reviews of Modern Physics*, vol. 74, article 99, 2002.
- [45] T. Cebeci, *Convective heat transfer*, Horizons Publishing Inc., Long Beach, CA; Springer-Verlag, Berlin, 2002.
- [46] J. E. Carter and J. Soria, "The evolution of round zero-net-mass-flux jets," *Journal of Fluid Mechanics*, vol. 472, pp. 167–200, 2002.
- [47] J. Soria, "Experimental studies of the near-field. Spatio-temporal evolution of zero-net-mass-flux (ZNMF) jets," in *Vortex Rings and Jets, Fluid Mechanics and Its Applications*, vol. 111, pp. 61–92, Springer, 111, 2015.
- [48] A. Glezer and M. Amitay, "Synthetic jets," in *Annual review of fluid mechanics*, Vol. 34, vol. 34 of *Annu. Rev. Fluid Mech.*, pp. 503–529, Annual Reviews, Palo Alto, CA, 2002.
- [49] H. Wang and S. Menon, "Fuel-air mixing enhancement by synthetic microjets," *AIAA Journal*, vol. 39, no. 12, pp. 2308–2319, 2001.
- [50] B. L. Smith and A. Glezer, "Jet vectoring using synthetic jets," *Journal of Fluid Mechanics*, vol. 458, pp. 1–24, 2002.
- [51] A. Pavlova and M. Amitay, "Electronic cooling using synthetic jet impingement," *Journal of Heat Transfer*, vol. 128, no. 9, pp. 897–907, 2006.
- [52] L. N. Cattafesta III and M. Sheplak, "Actuators for active flow control," *Annual Review of Fluid Mechanics*, vol. 43, pp. 247–272, 2011.
- [53] E. DeMont and J. Gosline, "Mechanics of jet propulsion in the hydromedusan jellyfish, *polyorchis penicillatus*," *Journal of Experimental Biology*, vol. 134, pp. 347–361, 1988.
- [54] <https://nek5000.mcs.anl.gov/>.
- [55] C. H. K. Williamson, "Oblique and parallel modes of vortex shedding in the wake of a circular cylinder at low Reynolds numbers," *Journal of Fluid Mechanics*, vol. 206, pp. 579–627, 1989.
- [56] C. H. K. Williamson, "Vortex dynamics in the cylinder wake," *Annual Review of Fluid Mechanics*, vol. 28, pp. 477–539, 1996.
- [57] C. P. Jackson, "A finite-element study of the onset of vortex shedding in flow past variously shaped bodies," *Journal of Fluid Mechanics*, vol. 182, pp. 23–45, 1987.
- [58] M. Provansal, C. Mathis, and L. Boyer, "Bénard-von Kármán instability: transient and forced regimes," *Journal of Fluid Mechanics*, vol. 182, pp. 1–22, 1987.
- [59] D. Barkley and R. D. Henderson, "Three-dimensional Floquet stability analysis of the wake of a circular cylinder," *Journal of Fluid Mechanics*, vol. 322, pp. 215–241, 1996.
- [60] D. Barkley, L. S. Tuckerman, and M. Golubitsky, "Bifurcation theory for three-dimensional flow in the wake of a circular cylinder," *Physical Review E: Statistical, Nonlinear, and Soft Matter Physics*, vol. 61, no. 5, part A, pp. 5247–5252, 2000.

- [61] H. M. Blackburn, F. Marques, and J. M. Lopez, "Symmetry breaking of two-dimensional time-periodic wakes," *Journal of Fluid Mechanics*, vol. 522, pp. 395–411, 2005.
- [62] J. M. Pérez, S. L. Clainche, and J. M. Vega, "Alternative three-dimensional instability analysis of the wake of a circular cylinder," in *Proceedings of the 8th AIAA Theoretical Fluid Mechanics Conference*, 2017, USA, June 2017.
- [63] G. Ramos, V. Beltrán, S. Le Clainche, E. Ferrer, and J. M. Vega, "Flow structures in the turbulent wake of a cross-flow wind turbine," in *Proceedings of the Wind Energy Symposium*, 2018, USA, January 2018.
- [64] S. Le Clainche, X. Mao, and J. M. Vega, "Spatio-temporal Koopman Decomposition in offshore wind turbines," in *Proceedings of the International Symposium on Transport Phenomena and Dynamics of Rotating Machinery (ISROMAC)*, Maui, Hawaii, 2017.
- [65] V. Beltrán, S. Le Clainche, and J. M. Vega, "Characterization of the Wake past a Two-dimensional Multi-body Cylinder Arrangement," in *Proceedings of the 2018 AIAA Aerospace Sciences Meeting*, Kissimmee, Florida.
- [66] M. Harris, M. Hand, and A. Wright, "A Lidar for Turbine Control," Technical Report NREL/TP-500-39154, National Renewable Energy Laboratory (NREL), Golden, CO, USA, 2006.
- [67] C. J. Karlsson, F. Å. A. Olsson, D. Letalick, and M. Harris, "All-fiber multifunction continuous-wave coherent laser radar at $1.55 \mu\text{m}$ for range, speed, vibration, and wind measurements," *Applied Optics*, vol. 39, no. 21, pp. 3716–3726, 2000.
- [68] S. Le Clainche, L. Lorente, and J. M. Vega, "Wind Predictions Upstream Wind Turbines from a LiDAR Database," *Energies*, vol. 11, no. 3, pp. 543–558, 2018.
- [69] S. Le Clainche, F. Sastre, J. M. Vega, and A. Velázquez, "Higher order dynamic mode decomposition applied to post-process a limited amount of noisy PIV data," in *47th AIAA Fluid Dynamics Conference*, Denver, Co, 2017, AIAA paper 2017-3304.
- [70] S. Le Clainche, R. Moreno-Ramos, P. Taylor, and J. M. Vega, "New Robust Method to Study Flight Flutter Testing," *Journal of Aircraft*, pp. 1–8, 2018.
- [71] P. Charbonneau, "Stellar Dynamos," in *Solar and Stellar Dynamos*, vol. 39 of *Saas-Fee Advanced Courses*, pp. 187–214, Springer Berlin Heidelberg, Berlin, Heidelberg, 2013.
- [72] F. Garcia, M. Net, B. García-Archilla, and J. Sánchez, "A comparison of high-order time integrators for thermal convection in rotating spherical shells," *Journal of Computational Physics*, vol. 229, no. 20, pp. 7997–8010, 2010.
- [73] J. Sanchez, M. Net, and C. Simo, "Computation of invariant tori by Newton-Krylov methods in large-scale dissipative systems," *Physica D: Nonlinear Phenomena*, vol. 239, no. 3-4, pp. 123–133, 2010.
- [74] J. Sanchez and M. Net, "A parallel algorithm for the computation of invariant tori in large-scale dissipative systems," *Physica D: Nonlinear Phenomena*, vol. 252, pp. 22–33, 2013.
- [75] J. Sánchez, F. Garcia, and M. Net, "Computation of azimuthal waves and their stability in thermal convection in rotating spherical shells with application to the study of a double-Hopf bifurcation," *Physical Review E: Statistical, Nonlinear, and Soft Matter Physics*, vol. 87, no. 3, 2013.
- [76] S. Chandrasekhar, *Hydrodynamic and Hydromagnetic Stability*, Oxford University Press, London, UK, 1961.
- [77] S. Le Clainche, J. M. Pérez, and J. M. Vega, "Spatio-temporal flow structures in the three-dimensional wake of a circular cylinder," *Fluid Dynamics Research. An International Journal*, vol. 50, no. 5, 051406, 19 pages, 2018.

